SLOVAK UNIVERSITY OF TECHNOLOGY IN BRATISLAVA

Faculty of Electrical Engineering and Information Technology

Mgr. Jana Hrdá

Dissertation Thesis Abstract

Study of the doping effect on the properties of ultra-thin layers of 2D materials

Submitted to obtain the academic title of
„philosophiae doctor“, abbreviated as „PhD.“

In the doctorate degree study programme:	Physical Engineering
In the field of study:	Electrical and Electronics Engineering
Form of Study:	full time

Bratislava, June 2024

STU

Dissertation Thesis has been prepared at
Institute of Electrical Engineering, Slovak Academy of Sciences

Submitter: Mgr. Jana Hrdá
Institute of Electrical Engineering, Slovak Academy of Sciences
Dúbravská cesta 9, 841 04 Bratislava
Slovakia

Supervisor: Mgr. Michaela Sojková, PhD.
Institute of Electrical Engineering, Slovak Academy of Sciences
Dúbravská cesta 9, 841 04 Bratislava
Slovakia

Readers: doc. Ing. Miroslav Mikolášek, PhD.
Institute of Electronics and Photonics
Ilkovičova 3, 812 19 Bratislava
Slovakia

RNDr. Milan Sýkora, MBA, PhD.
Laboratory for Advanced Materials
Comenius University Science Park
Ilkovičova 8, 841 04 Bratislava
Slovakia

Dissertation Thesis Abstract was sent: .....
(*Date of sending*)

Dissertation Thesis Defence will be held on .....

at.....**h** *(am/pm)* at Institute of Electrical Engineering, Slovak Academy of Sciences

Prof. Ing. Vladimír Kutiš, PhD.
Dean of Faculty of FEI STU

Table of Content

1. Introduction – Transition Metal Dichalcogenides

The rapid reduction in the size of electronic devices presents significant challenges for silicon-based microelectronics in the sub-10 nm range. To address the constraints of silicon-based electronics, the exploration of new semiconductor materials is needed. In recent decades, there has been a continuous investigation of new materials with the aim of either substituting or complementing silicon in electronic devices [1]. Layered 2D materials gained significant interest due to their exotic properties and possible applications in diverse areas, including channel transistors, logic devices, and memories [2]. Graphene is the most well-known and studied 2D material [3]. Despite its exceptionally high carrier mobility, monolayer and bilayer graphene lack a pristine band gap, which constitutes a primary drawback in applications. Nonetheless, the limitations of graphene prompted the exploration of other inorganic layered materials, including hexagonal boron nitride, silicene, borophene, MXenes, or transition metal dichalcogenides [4]. One of the most promising classes of layered materials is transition metal dichalcogenides (TMDs), characterized by the general formula "MX_2", where M stands for transition metal from groups 4 – 10, and X represents chalcogen. TMDs have a crystal structure consisting of hexagonal layers of metal atoms sandwiched between two layers of chalcogen atoms. In-plane exist strong covalent bonds, while adjacent layers are bonded together only by the van der Waals interactions [5], which allows prepare them in monolayer or few-layer form. TMDs could have a vast array of atomic combinations and diverse phases, including 1T (octahedral symmetry), 2H (trigonal prismatic coordination), and 3R (rhombohedral symmetry). TMD family encompasses insulators (e.g., $HfSe_2$), semiconductors (e.g., MoS_2, WS_2), semi-metals (e.g., WTe_2), genuine metals (e.g., VSe_2), and even superconductors (e.g., NbS_2, $NbSe_2$). The range of electrical conduction properties is attributed to the existence of a non-bonding *d* band and its filling state [6]. Fig. 1 displays crystal structure of 2H-MoS_2 and 1T-$PtSe_2$.

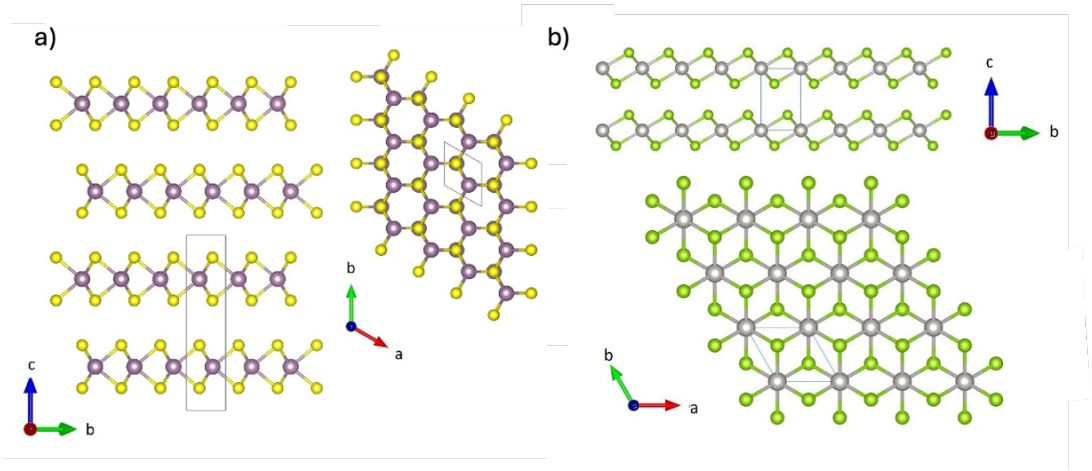

Figure 1: Side and top view of crystal structure belonging to (a) 2H-MoS_2 and (b) 1T-$PtSe_2$

Exploring TMD materials led to interesting findings about their band structure, which changes dramatically with the number of monolayers. Bulk semiconducting TMDs have an indirect bandgap while thinning to a monolayer, becoming a direct semiconductor [5]. The bulk MoS_2 has an indirect bandgap of 1.2 eV, changing to the direct bandgap of 1.9 eV as the monolayer [7]. Similar dependence of electronic structure on the thickness was also observed for $PtSe_2$. The bulk crystal of $PtSe_2$ shows semi-metallic characteristics, although after thinning down

to a few monolayers, it became a *p*-type semiconductor. Nonetheless, reported values of bandgap are not quite uniform. For monolayer $PtSe_2$, reported values range from 1.05 to 2.48 eV, and values for bilayer fall within the range of 0.21 - 0.80 eV [8]. Observed dependence of electronic structure on number of monolayers underscores the critical role of interlayer coupling. Furthermore, the electronic properties of TMDs are very sensitive to external conditions such as pressure, temperature, pressure, or strains. Therefore, the band structure and consequently the properties of TMDs might be tuned used various approaches - defect engineering, applying strains, doping, intercalation, or using external fields [5].

In our work we will focus on the fabrication and investigation properties of Li-doped MoS_2 and $PtSe_2$ thin layers. For $PtSe_2$ we have examined the role of stoichiometric Se:Pt ratio on the electrical properties.

2. Present State of the Problematics

2.1 Fabrication of TMDs:

Several fabrication techniques have been developed and can be divided into two main approaches – top-down and bottom-up. In the top-down approach, the bulk crystals are exfoliated into few-layer or monolayer structures. The second bottom-up approach uses growth methods such as molecular beam epitaxy, atomic layer deposition, pulsed laser deposition, chemical vapor deposition or thermally assisted conversion.

The top-down fabrication techniques include mechanical and liquid exfoliation. The mechanical exfoliation process was successfully used to fabricate single-layer graphene [3], and later, it was used in other layered inorganic materials, including MoS_2 [9]. This principle uses adhesive Scotch tape to peel off thin crystals of a bulk TMD crystal. Then, the tape is placed in contact with the chosen substrate and pressed down. Upon removal of the tape, the TMD flakes or nanosheets remain on the surface of the substrate. Flakes can vary in size and thickness, typically ranging from a monolayer to a few layers. Scheme of mechanical exfoliation and optical images of prepared flakes are shown in Fig.2 [10]. To date, mechanical exfoliation is the most efficient way to produce the highly crystalline atomically thin nanosheets of layered materials. Despite this, the exfoliation method does not allow any systematic control of flake size and thickness. In conclusion, mechanical exfoliation is more suitable for fundamental characterization and research than for large-scale production of TMD monolayers for industrial application. Other exfoliation approach is a liquid exfoliation using ion intercalation. The typical procedure involves bulk TMD powder submerging in a lithium-containing compound (e.g., n-butyl lithium) solution. Fabrication of nanosheets of certain TMDs through Li intercalation includes a phase transition [11], which is the main obstacle, along with the flakes' limited size and their overlapping.

As an illustration of bottom-up approaches we will discuss the pulsed laser deposition (PLD), chemical vapor deposition (CVD) and thermally assisted conversion (TAC). PLD is based on physical vapor deposition in a high vacuum. High-power laser pulses ablate the target and generate the plasma plume. Species get transferred to the substrate surface and crystalize. The PLD growth is independent of the partial pressures of the individual cations. The additional advantage is the stoichiometric transfer of ablated material to the substrate. TMD thickness is tuned by controlling the frequency of laser pulses, alternatively by laser energy or deposition pressure,

which can be used to modify the mean free path of ablated particles. The PLD-deposited TMDs thin films are of high quality and have a large area [12].

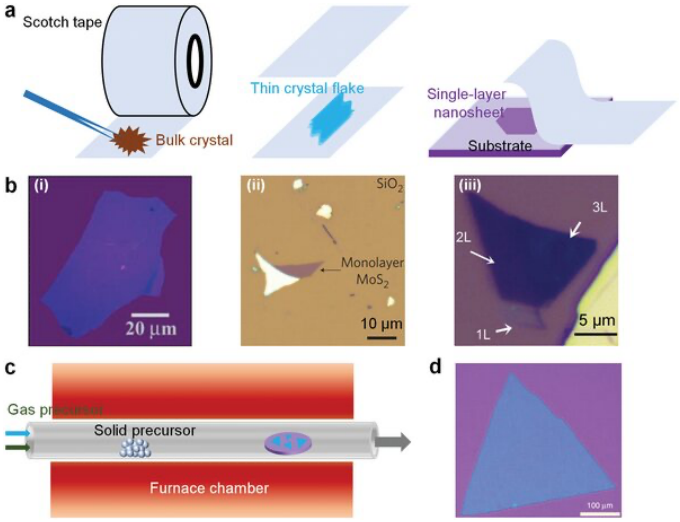

Figure 2: Principle of TMD nanosheets fabrication and their corresponding optical images prepared using (a-b) Scotch tape exfoliation and (c-d) CVD growth.

CVD is versatile and mostly used method to prepare various TMD materials. Deposition from the vapor phase could have several different approaches, using either gaseous precursors of metal or chalcogens or their powders. CVD don't require ultra-high vacuum, which makes it considerably more cost-effective and easily adaptable to the existing industrial process. Furthermore, CVD allows scalable production of large-area sheets, a critical requirement for future application [13]. The charge carrier mobility is the most crucial parameter for electronic and optoelectronic applications. The TMDs prepared by CVD growth have lower charge carrier mobility than exfoliated flakes due to the numerous defects or grain boundaries, which serve as scattering centers.

TAC is a method in which the metal/metal oxide layer is converted into TMD by introducing vapor-phase chalcogen. This method might be considered part of CVD. Regarding the chalcogen used, TAC is often called sulfurization, selenization or telurization Using TAC is possible to purposely change the crystallographic alignment of a few layers of MoS_2 and other TMDs by changing annealing parameters [14]. Such orientation tuning is desirable for intended applications. For instance, the horizontally aligned MoS_2 (layers are parallel to the substrate surface) is suitable for applications in electronics or optoelectronics. In contrast, the vertically aligned MoS_2 (layers are perpendicular to the substrate surface) is applicable in hydrogen evolution reactions or solar cells [14]. The main challenges of TAC are linked to lower grain dimensions resulting in lower charge carrier mobility of prepared TMDs. However, modification methods can enhance properties of fabricated TMDs.

2.2 Defect engineering:

Synthesis by chemical methods incorporates various structural defects like vacancies, dislocations, and grain boundaries. The study of the defects in the TMDs was focused mainly on the MoS_2 and its phases. Most point defects can be defined as vacancies and antisite defects. In general, it was reported that chalcogen single vacancy (V_X) was the most populous point defect in TMDCs. However, chalcogen double vacancy (V_{X2}) or metal vacancies (V_M) were also observed.

The electrical role of sulfur vacancies in MoS_2 is still questionable. Early stages of research believed sulfur vacancies contribute to the *n*-type doping effect. However, theoretical studies have not confirmed these experimental results, which opens the way for new approaches. Some studies suggest that the vacancies might act as acceptors and thus produce *p*-type doping. Other studies indicated that vacancies form traps at the neutral level, which results in electrostatic effects. A recent study of transient current measurement performed by Juchan Lee et al. [15] revealed that sulfur vacancies induce deep- and shallow-level traps. This indicates that sulfur vacancies could

not act as direct doping elements (donors or acceptors). Instead, the holes become ensnared at these deep trap sites and persist for an extended duration. Trapped holes had a positive charging effect, which enhanced electron generation within the channel. Consequently, sulfur vacancies seem to induce an *n*-type of doping impact, which agrees with early research observations.

Hu Xu et al. [16] proposed $PtSe_2$ thin films with p-type and n-type conductivity using different selenization properties. A deficiency of Se in stoichiometry composition led to n-type conductivity. On the other hand, the slow cooling process with continuous Se precursor supply led to the Se:Pt ratio of about 2.24 and p-type of conductivity.

2.3 Doping/Intercalation of TMDs

The ability to introduce impurity elements and dope semiconductors with proper carriers is crucial for their successful implementation in practical devices. For TMDs, substitutional doping proves higher stability than charge transfer doping by surface adsorbates, which are susceptible to thermal desorption. Impurity atoms may substitute either metal or chalcogen sites and act as donors or acceptors, depending on their relative valency [17].

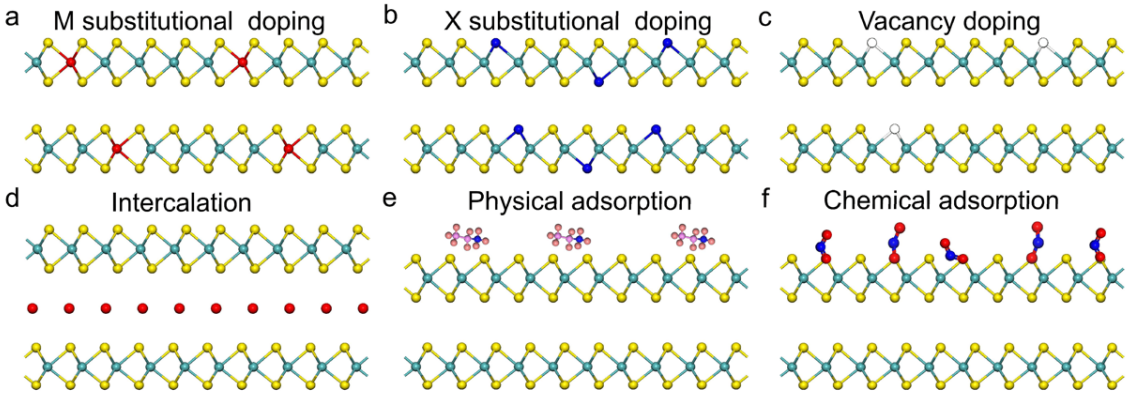

Figure 3: Schematic diagram of different doping types. The yellow and blue balls in the schematic stand for the intrinsic atoms in TMDs. (a,b) M and X substitutional doping, the red and navy-blue balls represents M substitutional atoms and X substitutional atoms, respectively. (c) Vacancy doping formed in TMDs. (d) Atom or molecular intercalation formed in the van der Waals gaps The red balls correspond to the intercalated atoms or molecules. (e,f) Physical and chemical adsorption formed on the surface of TMDs [18].

On the other hand, the intrinsic van der Waals gap allows to intercalate species. Intercalation species in the vdW gap of TMDs modify the properties of TMDs through many effects, including charge doping, orbital hybridization, expansion of the c lattice constant, phonon scattering, or introducing disorder. By this, a vast range of properties can be tuned, such as electrical conductivity, optical modes, magnetic order, catalytic activities, or energy storage and conversion performance. Intercalants can be categorized into three groups: (1) Alkali metal atoms + groups II, XIII, and XIV elements; (2) Transition metals; (3) Organic molecules [19].

Different effects can change the electronic properties of TMDs—the first is charge transfer from intercalants to the host atoms, and the second is associated with lattice modulation (transfer from 2H phase to 1T phase) [19]. Phase engineering might be useful for reducing contact resistance in device fabrication. Kappera et al. [20] reported on the top-gated FET device with a 2H-phase MoS_2 channel, while the 1T-MoS_2 edges were used for Au-contacting electrodes. The device with 1T/metal contacts proved low resistance, which increased mobility values and the on/off ratio compared to the device using only a 2H/metal interface.

2.4 Applications:

One of the primary attractions of 2D crystals lies in their potential as conduction channels in digital circuits beyond the silicon. The pioneering work of Radisavlejic et al. [9] reported a FET consisting of a micro-mechanically cleaved single-layer MoS_2 on the top of the Si/SiO_2 substrate, using gold electrodes and 30 nm HfO_2 as the gate insulator. The scheme of the device is in Fig. 4. The device exhibited n-type conductivity, with a room-temperature current on/off ratio of 108 and mobility of 200 $cm^2\ V^{-2}\ s^{-1}$. On the other hand, devices fabricated using MOCVD/CVD still show significantly smaller charge mobilities.

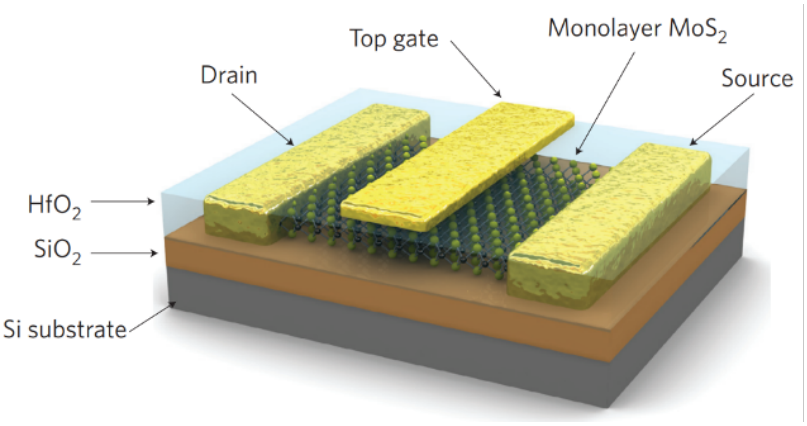

Figure 4: Scheme of top-gated monolayer MoS2 field effect transistor [10].

Zhao et al. [21] reported for the first time a FET device with a CVT-grown $PtSe_2$ channel. The few-layer $PtSe_2$ device exhibited semiconducting behavior and achieved room-temperature electron mobility of 210 $cm^2\ V^{-2}\ s^{-1}$ in a back-gated configuration. The device using bulk $PtSe_2$ exhibited metallic-like behavior. Xu et al. [16] investigated both n-type and p-type FETs fabricated from $PtSe_2$ grown by the selenization of Pt films. FET mobilities were 14 $cm^2\ V^{-2}\ s^{-1}$ and 15 $cm^2\ V^{-2}\ s^{-1}$ for p-type, n-type $PtSe_2$ device respectively. Notably, the performance of both types is nearly symmetric. The p-type $PtSe_2$ was grown by over-selenization, meaning the Se precursor was supplied during the slow cooling process, which led to an increased Se:Pt ratio to 2.45. Oppositely, n-type conductivity was achieved selenization with a rapid cooling process. In this case, the Se:Pt ratio was only 1.96.

TMDs including MoS_2 and $PtSe_2$ find their applications in optoelectronic devices, sensors or electrocatalytic devices [2,8].

3. Objectives of the Dissertation Thesis

- Fabrication of lithium-doped MoS_2 few-layer films using a one-zone sulfurization method with Li_2S as a lithium source. Using both molybdenum and molybdenum disulfide layers for the doping.
- Detection of the lithium amount using Synchrotron radiation X-ray photoemission spectroscopy (XPS) and Elastic Recoil Detection Analysis (ERDA)
- Study the influence of the growth parameters (annealing temperature and time, amount of Li_2S used) and the initial layer (Mo, MoS_2) thickness on the structural and optical properties of the doped films. Characterization of the films using XRD measurements, GIWAXS (grazing-incidence wide-angle X-ray scattering), Raman spectroscopy, and optical measurements. The measurements aim to determine the correlations between the structural and optical properties of the doped layers and the lithium content in the sample.
- Monitoring the dependence of electrical conductivity and charge carrier mobility on the concentration of Li in MoS_2 layers. Measurements of the temperature dependence of doped layers determination of the mechanism of electrical conductivity of thin layers.
- Fabrication of undoped and over-doped $PtSe_2$ films. Study of the influence of stoichiometry on the electrical properties of the final films.
- Fabrication and study of lithium-doped $PtSe_2$ (or other TMD) thin films.

4. Experimental methods

4.1 MoS_2 and $PtSe_2$ fabrication:

The thermally assisted conversion was used to fabricate both MoS_2 and $PtSe_2$ few-layer films. In the first step, thin metal layers were deposited on the top of the c-plane sapphire substrate using homemade DC magnetron sputtering from Mo or Pt targets at room temperature in an argon atmosphere. Pressure during sputtering was 10^{-3} mbar, and the DC power and emission current were 460 W, 0.3 A, and 580 W, 0.18 A, respectively, for Mo and Pt deposition. The sample holder's rotation speed controlled the deposited layers' thickness. Thicknesses of sputtered Mo and Pt layers ranged from 1 nm to 10 nm.

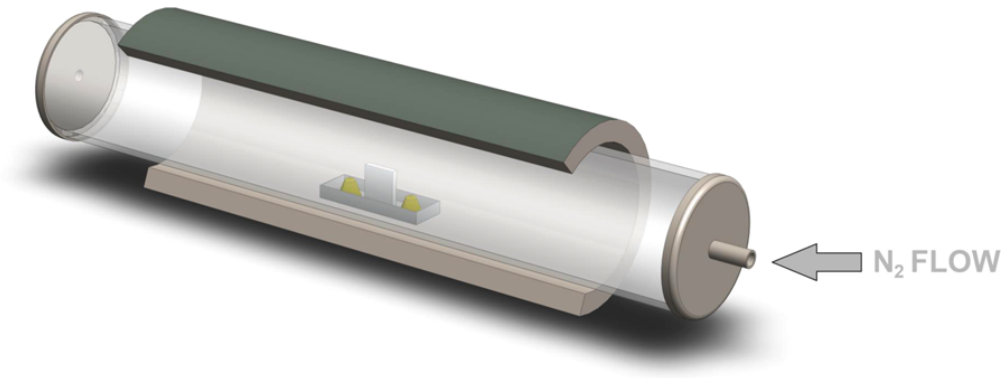

Figure 5: Schematic of the custom-designed TAC chamber, quartz crucible with chalcogen powder, and the pre-deposited metal film placed in the middle of the furnace [91].

In the second step We used a custom-designed one-zone furnace (Fig. 5). The substrate with pre-deposited (Mo, Pt) was inserted into the quartz crucible alongside the chalcogen (S, Se) powder and placed in the middle of the one-zone furnace. The furnace was connected to the gas supply. For the growth, we used nitrogen flow with different flow rates. The thin metal layers were annealed in chalcogen vapors in a nitrogen atmosphere at ambient pressure. The sulfurization temperature was 800 °C for the fabrication of MoS_2, and the selenization temperature was 550 °C for the fabrication of the $PtSe_2$ thin films. The heating rate was set to 25 °C/min for both chalcogenizations. The maximum temperature was held for 30 minutes, followed by spontaneous cooling.

MoS_2 layers were also grown by the pulsed laser deposition (MBE/PLD-2000 system). The system consisted of a KrF excimer laser emitting at a wavelength of 248 nm, optical mirrors, and a focusing lens. A laser pulse with an energy of 70 mJ, operating at a repetition rate of 4 Hz and with a spot size of 2 mm^2, ablated the stoichiometric MoS_2 target. The sample holder was heated at 800 °C; however, the real growth temperature on the substrate was about 600 °C, and the growth pressure was $2.6 \cdot 10^{-6}$ mbar. Following film growth, samples were cooled to 200 °C at a rate of 50 °C/min and then cooled naturally. This rapid cooling helped reduce sulfur desorption from the resulting MoS2 thin film. The final thickness of the MoS2 film was controlled by the number of pulses, typically within the range of 400 to 800 pulses.

4.2 Li-doping of thin films:

For doping, we used a method called solid-state diffusion. The Mo/MoS_2 thin film sample was placed in the middle of the one-zone reactor alongside a mixture of chalcogen and lithium sulfide (Li_2S) powders. Li_2S is a compound that melts at the temperature of 938 °C. The doping

temperature was set to 600 °C or 800 °C. In the presence of a sulfur reduction atmosphere, Li_2S undergoes evaporation. Applying the annealing temperature of 800 °C, there were no Li_2S residues in the crucible after annealing.

We have tested two approaches to fabricating Li-doped large-area (~ cm^2) MoS_2 samples. In the first one, the pre-deposited Mo layer was sulfurized in a mixture of sulfur and Li_2S powders. The heating rate was 25 °C/min, the growth temperature was set to 800 °C, and it was kept for 30 minutes. Nitrogen flow was set to 100 sccm. The second approach uses already-grown MoS_2 layers, which were annealed in a mixture of S/Li_2S powders. Initial MoS_2 layers were grown either by the sulfurization of Mo thin films or PLD. The heating rate was 25 °C/min, and the maximum temperatures were 600 °C and 800 °C for PLD and TAC-grown initial MoS_2 layers, respectively. The maximum temperatures were kept for 30 minutes and cooled naturally. Two varying quantities of Li_2S (0.1 and 0.25 g) were employed, substituting 20% and 50% of the sulfur powder, respectively.

4.3 Characterization techniques:

Our samples were characterized using different techniques, including Raman spectroscopy, X-Ray Diffraction (XRD), Grazing-Incidence Wide-Angle X-ray Scattering (GIWAXS), Atomic Force Microscopy (AFM), synchrotron-based X-ray Photoelectron Spectroscopy (XPS), Elastic recoil detection analysis (ERDA), Hall measurements, R(T) measurements and optical characterization.

Raman spectra of studied samples were obtained at ambient conditions by a confocal Raman microscope (Alpha 300R, WiTec, Germany). A 532 nm wavelength laser was used, with a laser power below 1 mW to prevent sample damage. The scattered Raman photons were gathered using a 50× (NA= 0.8) microscope objective and detected by a Peltier-cooled EMCCD camera. A blazed grating with 1800 grooves per minute was employed for dispersing the Raman spectra. The spectral resolution of the system used is approximately 0.75 cm^{-1}.

XRD analysis was performed with a diffractometer Bruker D8 DISCOVER equipped with a rotating anode (Cu Kα) working at a power of 12 kW. The diffraction patterns were measured using a symmetric $2\theta/\theta$ configuration. Diffractograms were recorded in the interval of 2θ from 10° to 35°. The in-plane crystallographic orientation of films was studied by the azimuthal φ-scan concerning the sapphire substrate. Additionally, the out-of-plane texture was investigated by the ω-scan.

GIWAXS measurements performed in our experiment were done on the home-built system consisting of the microfocus X-ray source (IμS, Incoatec GmbH, Germany) using focusing Montel optics, sample holder with attached hexapod (H-811.S2, Physik Instrumente, Germany) and CMOS-based X-ray 2D detector (Pilatus 200K, Dectris, Switzerland). The power of the microfocus X-ray source was 30 W (voltage of 50 kV and current was 600 μA), which generates Cu Kα radiation with energy 8.04 keV ($\lambda = 1.54$ Å) and a photon flux of approximately 3×10^8 photons/s. The examined sample was placed in the hexapod with 6 degrees of freedom to ensure the grazing-incidence geometry. The incidence angle was set to 0.2°. The detector collecting GIWAXS patterns had the size of 498 × 407 pixels (with the size of 172 × 172 μm^2). The sample-detector distance (SDD) was validated by a calibration standard (corundum) and

determined to be about 50 mm. All measurements were conducted in ambient conditions, and each GIWAXS pattern was collected using an exposure time of 600 seconds.

AFM: MoS_2 samples were measured on HR-AFM (BrukerNano, Multimode 8), with a tip radius of 2 nm, to achieve the best possible resolution. A one-dimensional autocorrelation function (ACF) was performed on the data. The fitting parameters of ACF correspond to RMS surface roughness and correlation length. The grain-size distribution was obtained as well.

XPS experiments were conducted at the BACH beamline at Elettra synchrotron in Trieste, Italy. The main advantage of synchrotron-based XPS is the wide range of tunable photon energies. We needed lower photon energies for Li detection. The beamline was equipped with an R3000 hemispherical analyzer at 60° relative to the X-ray incidence direction. The samples were degassed in a vacuum at a temperature of 250 °C for 10 minutes before the measurements. The spectra were recorded in a normal emission geometry.

ERDA measurements of our samples were carried out in Helmholtz-Zentrum Dresden-Rossendorf. In the initial batch of samples, a 43 MeV Cl^{7+} ion beam was employed, with recoil atoms and scattered ions detected at a scattering angle of 29.5° using a Bragg ionization chamber. H and Li recoils were identified using a separate solid-state detector at a scattering angle of 40°. This detector contained a 25 μm Kapton foil to stop scattered and heavy recoil ions. Another batch of samples was analyzed by a 15 MeV Cl^{4+} beam, and recoils and ions were detected at a scattering angle of 40° employing a time-of-flight – energy (ToF-E) telescope.

Hall measurement consisted of an electromagnet with a tunable magnetic field up to 1T, powered by a high-power source. The constant current was produced by the current source Keithley 2400, and a Keithley 2700 multi-meter was used for measuring the voltages.

Resistance vs. Temperature R(T) measurements of MoS_2 and Li-doped MoS_2 samples' was acquired using the four-probe method using the Physical Property Measurement System – Model 6000, from Quantum Designed Inc. Gold contacts were patterned using photolithography (lift off method) and deposited by the thermal evaporation on the top of the samples. The distance between contacts was 10 μm.

Optical characterization of our films was done by collecting reflectance and transmittance spectra measured with Shimadzu SolidSpec-3700 spectrophotometer in the UV–VIS range.

5. Results and discussion

5.1 Undoped MoS_2 layers fabricated by TAC

The MoS_2 films were grown by the TAC method from 1, 3, and 10 nm Mo films. The Raman spectroscopy confirmed the formation of 2H-MoS_2. Figure 6a shows the normalized Raman spectra containing characteristic in-plane E^1_{2g} (~383 cm^{-1}) and out-of-plane A_{1g} (~408 cm^{-1}). The thicknesses of the samples were estimated from XRR to 4, 12 and 40 nm. To obtain information about the orientation of the as-prepared MoS_2 films, GIWAXS measurements were performed. GIWAXS provides statistical average information over a significant sample' area. In Fig. 6b, for the thinnest 4 nm MoS_2 sample, only one diffraction spot at $q_z \sim 1$ $Å^{-1}$ is visible, indicating that the layers are aligned horizontally (basal planes are parallel to the substrate). For thicker films, 12 and 40 nm MoS_2 (Fig 6.4c and 6.4d, respectively), two diffraction spots are present at $q_{xy} \sim 1$ $Å^{-1}$, indicating the vertical alignment of the layers. The azimuthal φ-scans of as-prepared MoS_2 layers did not show any tendency of ordered growth in the a-b plane.

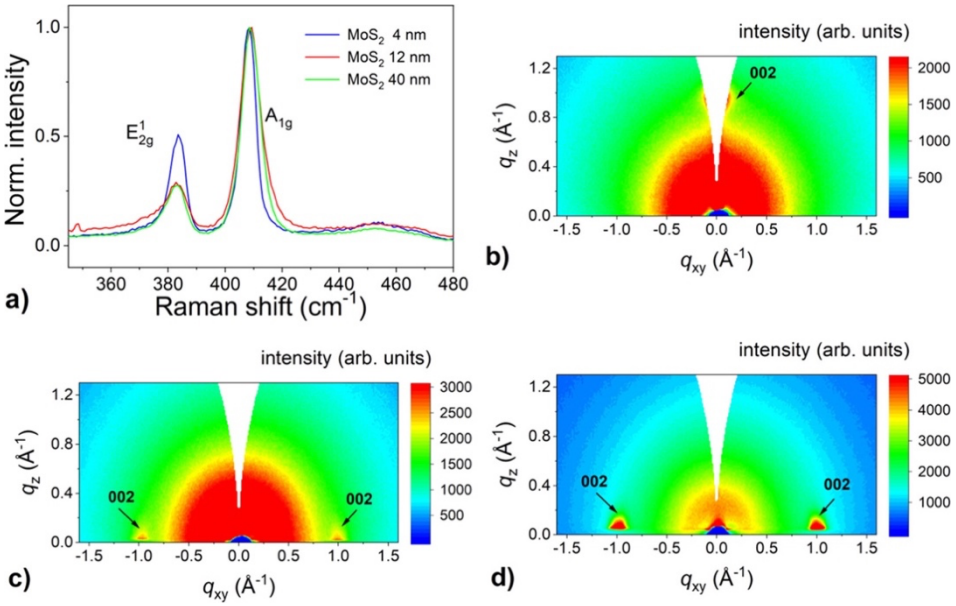

Figure 6: (a) Normalized Raman spectra of undoped MoS_2 films with different thicknesses grown by one-zone sulfurization at 800 °C for 30 min on the c-plane sapphire substrate. Corresponding GIWAXS reciprocal space maps of 4 nm (b), 12 nm, (c) and 40 nm (d) thick MoS_2 films.

5.2 Fabrication of Li-doped MoS_2 starting from Mo film (two-step synthesis)

Li-doped MoS_2 films were prepared similarly to undoped films. In the first step, Mo with thicknesses of 1, 3, and 10 nm was deposited on the c-plane sapphire substrate. The second step is sulfurization, where part of sulfur powder is replaced by Li_2S powder. The Li_2S was 20% (0.1 g) or 50% (0.25 g) of the total powder weight. The sulfurization parameters were the same as in the case of the fabrication of undoped MoS_2 layers.

The Mo conversion to MoS_2 was confirmed using Raman spectroscopy for both concentrations of Li_2S. In the normalized Raman spectra (Fig. 7a-b) are present characteristic peaks of MoS_2, namely E^1_{2g} and A_{1g}. The differing intensities of the E^1_{2g} peak in normalized spectra indicate varied orientations of the MoS_2 layers, particularly noticeable for 40 nm thick Li-MoS_2 prepared at two different nominal Li_2S concentrations.

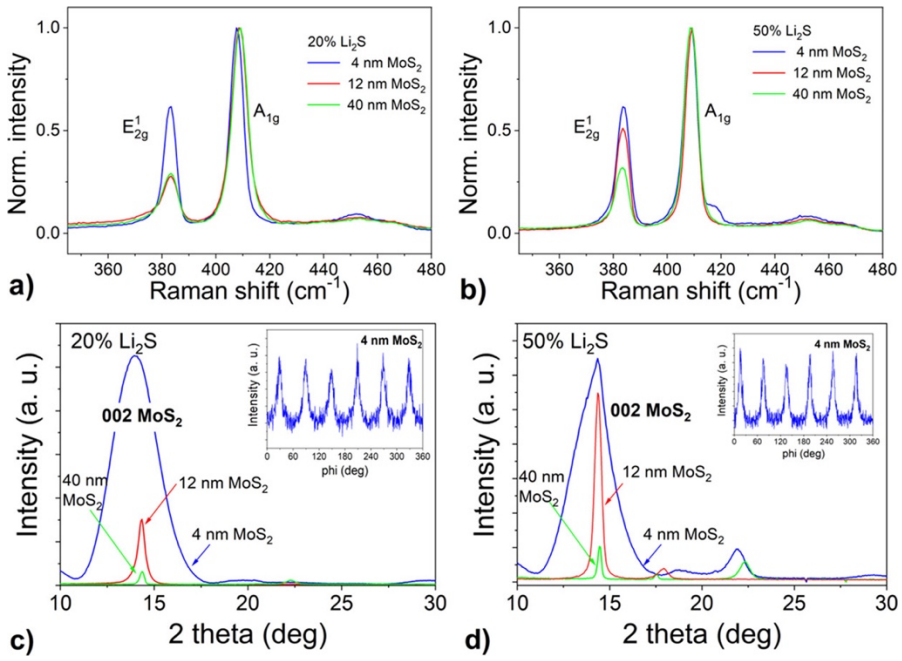

Figure 7: Normalized Raman spectra of Li-doped MoS_2 prepared from Mo films of different thicknesses using one-zone sulfurization at 800 °C for 30 min with 20% (a) and 50% (b) Li_2S portion. XRD patterns of the same films with 20% (c) and 50% (d) Li_2S portion. Azimuthal φ-scans of 103 diffraction of 4 nm lithiated MoS_2 are shown as insets.

The XRD was used to examine the crystal structure of the as-prepared films (Fig. 7c-d). For 4 nm Li-doped MoS_2 films, a broad 002 diffraction peak of 2H-MoS_2 is present in the pattern (with FWHM over 2°). This broadening can be attributed to the low film thickness. In the case of the thickest 40 nm films, the 002 diffraction has very low intensity, which suggests the prevalent horizontal alignment of the MoS_2 layers. For 12 nm MoS_2, the 002 diffraction peak is significantly greater in the sample prepared with 50% Li_2S, probably due to the different orientation of MoS_2 layers. Epitaxial growth was observed for the thinnest 4 nm MoS_2 samples prepared with both Li_2S concentrations. In the φ-scan patterns (insets of Fig. 7) six distinct peaks separated by 60° are present, confirming the epitaxial growth.

The orientation of Li-doped MoS_2 layers was investigated using GIWAXS measurements (Fig. 8). When a 3 nm thick initial Mo layer was used, vertically aligned films grew with less Li_2S and horizontally oriented Li-doped MoS_2 layers were obtained using 50% Li_2S concentration.

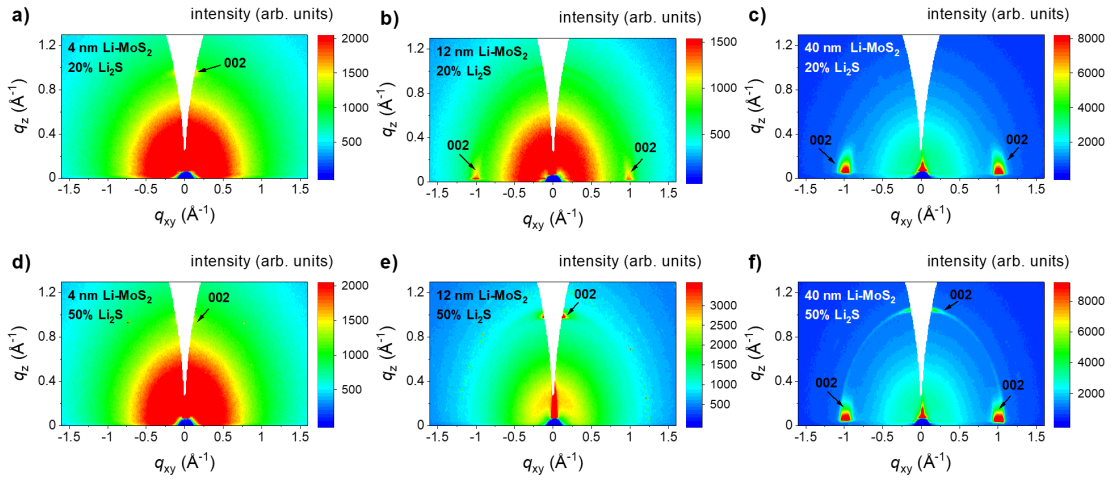

Figure 8: GIWAXS reciprocal space maps of Li-doped MoS2 films with different thicknesses grown by a two-step route using one-zone sulfurization at 800 °C for 30 minutes with (a-c) 20% and (d-f) 50% nominal Li2S concentrations.

5.3 Fabrication of Li-doped MoS_2 starting from MoS_2 layers (three-step synthesis)

The second approach of Li-doping involved already-grown MoS_2 as initial layers. The MoS_2 layers of different thicknesses prepared by TAC were annealed in the sulfur and Li_2S powders mixture under the same conditions as in the case of Mo initial layers. Again, two concentrations of Li_2S powders were used (20% and 50%).

Figure 9a-b shows the normalized Raman spectra of initial and Li-doped MoS_2 layers. The changes were only minimal in all cases, besides 12 nm Li-MoS_2, where the intensity of E^1_{2g} peak slightly increased compared to the undoped film for both Li_2S doping concentrations, suggesting orientation change. XRD investigation (Fig. 9c-d) shows similar results as in the case of two-step synthesis presented in the previous sub-chapter. In contrast, an intense and narrow 002 diffraction peak is present in the XRD pattern of 12 nm MoS_2 prepared with 20% and specifically with 50% Li_2S. This suggests a horizontal orientation of 12 nm MoS_2 films. Insets presents azimuthal φ-scans, showing ordering in the a-b plane for 4 nm and even for 12 nm Li-doped MoS_2 films.

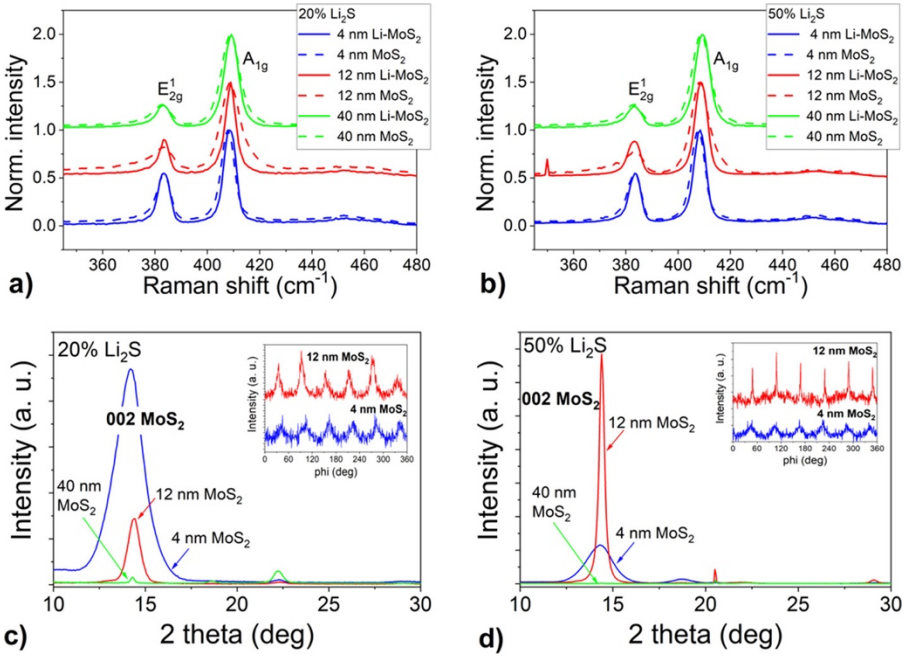

Figure 9: Normalized Raman spectra of Li-doped MoS_2 prepared from MoS_2 films of different thicknesses using one-zone sulfurization at 800 °C for 30 min with 20% (a) and 50% (b) Li_2S portion. XRD patterns of the same films with 20% (c) and 50% (d) Li_2S portion. Azimuthal φ-scans of 103 diffraction of 4 and 12 nm lithiated MoS_2 are shown as insets.

The alignment of the Li-doped MoS_2 layers was checked by the GIWAXS technique. GIWAXS reciprocal space maps are gathered in Figure 6.10. These measurements confirmed the horizontal orientation of 12 nm Li-doped MoS_2 samples, which has been expected from the Raman and XRD analysis. Three diffractions are visible for the thickest 40 nm samples – two at $q_{xy} \sim 1$ Å^{-1} and one at $q_z \sim 1$ Å^{-1}, meaning that the mixed horizontal and vertical orientations of hexagonal Li-MoS_2 layers were present for both doping concentrations. Anyhow, the initial undoped 12 nm MoS_2 films were vertically oriented, therefore we can conclude that Li doping induced conversion from the vertical to horizontal alignment of the layers.

To be sure, whether the lithium is the key factor of reorientation of already grown thicker MoS_2 layers, we performed an additional thermal annealing in a sulfur atmosphere without Li_2S powder on undoped MoS_2 samples. We did not spot any signs of reorientation upon GIWAXS examination. This experiment confirms lithium's role in the reorientation of the few-layer MoS_2

films. We performed also experiments with lower Li doping temperatures (400 °C and 600 °C); however, any change in the orientation was observed. We suppose that under certain conditions lithium acts as a catalyst and enables structural reorganization. This scenario is supported by the fact that we did not observe any change in the film orientation if the lithiation temperature was set to 600 °C.

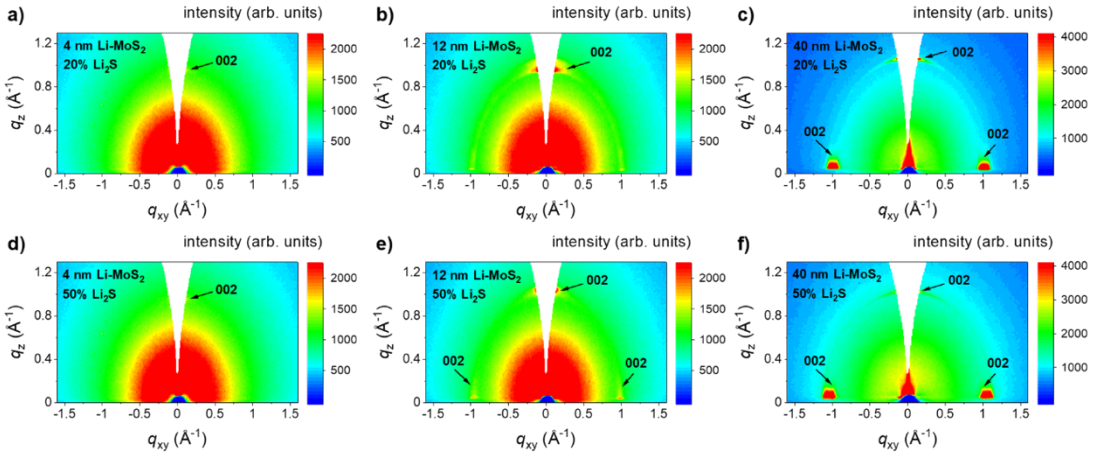

Figure 10: GIWAXS reciprocal space maps of Li-doped MoS_2 films with different thicknesses grown by a three-step synthesis using one-zone sulfurization at 800 °C for 30 minutes with (a-c) 20% and (d-f) 50% nominal Li_2S concentrations

5.4 Identification of Li content in Li-doped MoS_2

The chemical composition of our samples and verification of lithium content were checked by a combination of synchrotron-based X-ray photoemission spectroscopy, X-ray absorption near-edge structure, and Elastic Recoil Detection Analysis. XPS spectra were recorded at three photon energies – 120, 270, and 600 eV. Figure 11 displays Li 1s and Mo 4s XPS core-level spectra acquired at a photon energy of 270 eV from the Li-MoS_2 samples prepared using two-step and three-step methods. The Li 1s peaks in XPS spectra of 4 and 12 nm Li-MoS_2 exhibit a dominant component centered at a binding energy of 55.8 ± 0.1 eV, whereas the Li 1s peak for the 40 nm Li-MoS_2 sample is shifted to 56.4 ± 0.2 eV. The binding energy of 55.8 eV can be ascribed to Li atoms intercalated into MoS_2 [22]. The Li 1s peaks of our Li-MoS2 samples were also assigned by the Li K-edge XANES spectroscopy.

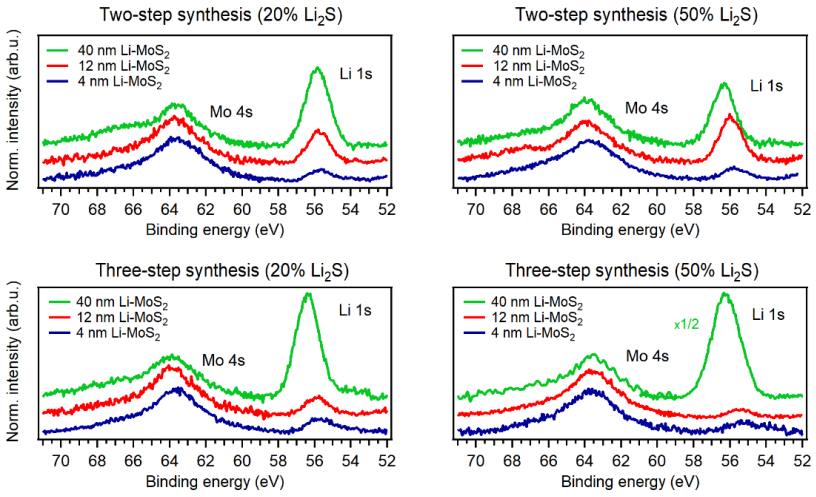

Figure 11: Li 1s and Mo 4s XPS spectra gathered from the surfaces of Li-doped films prepared by two-step (top) and three-step (bottom) sulfurization with a 20% (left) and 50% (right) portion of $L_{i2}S$. All spectra were acquired using a photon energy of 270 eV.

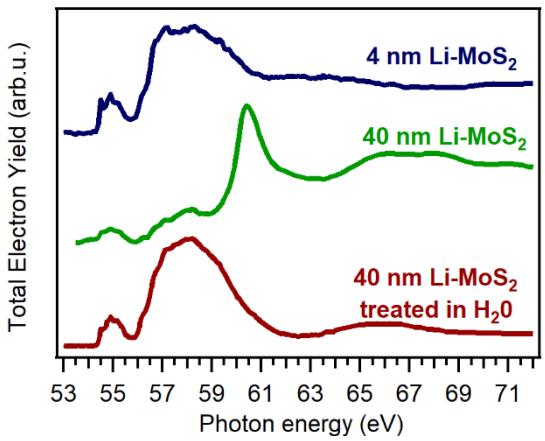

Figure 12: Li K-edge XANES spectra of Li-MoS_2 films fabricated using two-step synthesis. The lowermost spectrum was obtained from the 40 nm Li-MoS_2 sample after it was soaked in ultrapure water for a few minutes.

Li K-edge XANES spectra exhibit unique energy positions and line shapes for different lithium compounds, serving as distinctive signatures for identifying phase composition [23]. Figure 12 shows the Li K-edge spectra gathered from the 4 and 40 nm thick Li-doped MoS_2 samples. The Li K-edge spectrum observed in the 4 nm film has not been documented previously in the literature. Phases such as Li_2S, LiOH, Li_2CO_3, and Li oxides can be ruled out as they would display distinct features absent in the observed spectrum. Thus, we attribute the Li K-edge shape obtained from the 4 nm thick Li-MoS_2 film to lithiated MoS_2. Although the Li K-edge spectrum of the 40 nm thick sample is notably different. Weak features of Li-MoS_2 in the energy range from 55 to 58 eV are still discernible, while dominant features are visible between 60 and 70 eV, which might be attributed to Li_2SO_4 [24]. However, upon removal of the topmost surface layers, the 40 nm Li-MoS_2 exhibited a Li K-edge spectrum almost identical to that obtained for the thinner sample. This suggests that the thicker MoS_2 films also underwent lithiation like the thin ones. To validate our attribution of the observed Li K-edge XANES spectra to Li-MoS_2 we did theoretical investigation of the electronic structure of the unoccupied states of Li-doped MoS_2. The computed XANES spectra for Li atoms intercalated in tetrahedral and octahedral sites of MoS_2 accurately replicate the key experimental characteristics, including the main edge above 57 eV and the pre-edge region around 55 eV.

Lithium molar fraction was estimated by XPS from intensity ratios of peaks Mo 4s and Li 1s (Fig 11). The photon energies were kept below 600 eV to achieve sensitivity to Li 1s. However, the probing depth was limited to less than 4 nm. On the other hand, Li content examined by ERDA provided us with information from the whole samples' volume. The data from both techniques are summarized in Table 1.

Table 1: Atomic concentrations of Li_xMoS_2 determined by ERDA and XPS. Numbers determined by XPS are averaged values of depth profiling Li contend obtained by tuning photon energies.

MoS_2 layer thickness	**Li_2S amount**	**Two-step synthesis *x* (Li_xMoS_2)**		**Three-step synthesis *x* (Li_xMoS_2)**	
		ERDA	XPS	ERDA	XPS
4 nm	20 %	0.15	0.11 ± 0.04	0.14	0.13 ± 0.02
12 nm	20 %	0.04	0.3 ± 0.1	0.63	0.17±0.05
40 nm	20 %	0.05	n/a*	0.06	n/a*
4 nm	50 %	0.27	0.10 ± 0.03	2.20	0.10 ± 0.01
12 nm	50 %	0.08	0.41 ± 0.06	0.44	0.10 ± 0.05
40 nm	50 %	0.02	n/a*	0.02	n/a*

**n/a* values reflect the uneven depth distribution of Li near the surface observed by XPS

For the 4 nm Li-MoS_2 films prepared using 20% Li_2S are both ERDA and XPS results in good agreement. The 4 nm thick films prepared with a higher fraction of Li_2S showed higher lithium content within the film, as indicated by the ERDA results. This suggests that lithium is concentrated near the substrate, thus it is undetectable by XPS. Similar to the 12 nm Li-MoS_2

prepared by three-step synthesis, which was horizontally aligned with a-b plane ordering. We believe this structure facilitates lithium storage between the layers of MoS_2; however, we cannot rule out the formation of the Li-rich interface between the MoS_2 and the c-plane sapphire substrate. Conversely, the 12 nm Li-MoS_2 films synthesized in two steps exhibited less lithium in the bulk and higher concentrations near the surface. This reversed concentration profile could be due to different diffusion coefficients of Li in MoS_2 and metallic Mo. The 40 nm samples had a vertical orientation; therefore, intercalated Li was more accessible to air molecules. We believe it might cause Li segregation to the surface.

5.5. Comparison of TAC-grown and PLD-grown Li-doped MoS_2: from structural characterization to electron transport

For the electrical characterization we have used layers with predominant horizontal orientation, to obtain most ideal transport case. Studied undoped thin MoS_2 films were grown by two techniques TAC and PLD, which were subsequently annealed in the presence of Li_2S with two nominal concentrations 20% and 50%. Both initial MoS_2 layers were horizontally aligned and had comparable thickness. By the XRR method, the thickness of TAC samples was estimated to be 4 nm (corresponding to 5-6 ML) and PLD-grown samples were slightly thinner, about 3.5 nm (corresponding to 5 ML).

To be sure Li-doping did not caused phase transition from semiconducting 2H to metallic 1T, we checked our doped and undoped MoS_2 samples by various characterization techniques. Raman spectroscopy and XRD analysis proved formation of 2H-MoS_2 and horizontal orientation of MoS_2 layers for both, doped and undoped MoS_2 films. Moreover, the optical characterization was done by measuring the transmittance and reflectance from both the front and back sides of the sample. This method allows us to determine the absorbance of MoS_2 layers without assuming any specific model for the layer's dielectric function [25]. Fig. 13 presents the absorption spectra of the undoped, and Li-doped samples prepared with 50% Li_2S. All spectra are consistent with those reported for multi-layer samples with a similar number of MoS_2 monolayers [26]. All of them show an optical gap of 1.7 - 1.8 eV, which confirms that both the undoped and Li-doped samples are semiconductors.

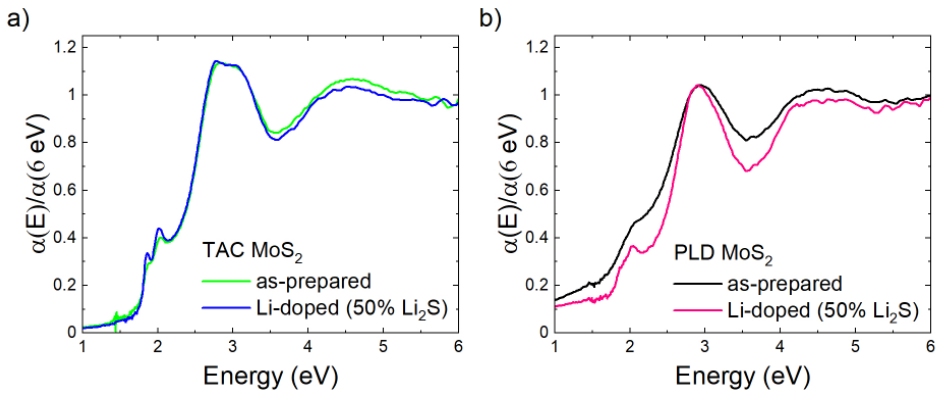

Figure 13: Absorbance of as-prepared and Li-doped MoS_2 samples grown by (a) TAC and (b) PLD method

The chemical composition and stoichiometry of the undoped and Li-doped MoS_2 were analyzed by synchrotron-based X-ray photoemission spectroscopy. Li 1s spectra (Fig. 14) verifying lithiation of both TAC and PLD-grown samples. Similarly, as discussed previously, the main component of Li 1s is centered at a binding energy of 55.08 ± 0.1 eV, attributed to Li

intercalation to MoS_2 layers [22]. The minor component at lower binding energies likely came from the presence of Li in hydroxide and oxide species [27,28]. The intensity ratio between Li 1s and Mo 4s peaks reflects the relative elemental atomic concentrations. The Li content x (Li_xMoS_2) and S:Mo stoichiometric ratio is gathered in Table 2 for all investigated CVD-grown and PLD-grown MoS_2 samples. It is noteworthy, that PLD-grown samples had stoichiometric Mo:S ratio close to 2, while the CVD-grown samples exhibited perturbated stoichiometry with S:Mo ratio approaching 2.2. Traces of other impurities and carbon contamination was likely without any special influence on the electron transport properties.

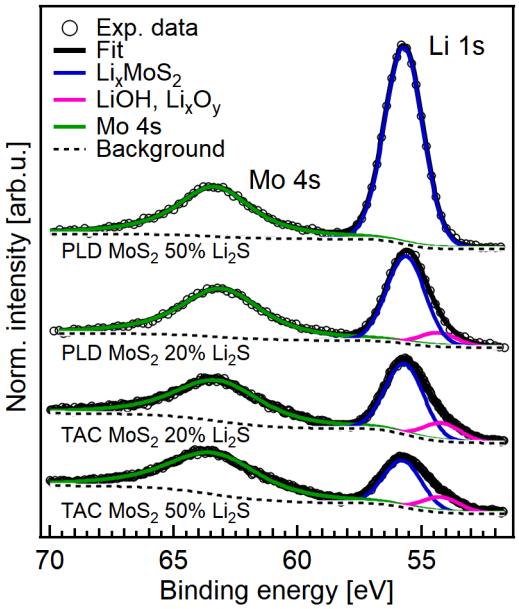

Figure 14: Li 1s and Mo 4s photoelectron spectra for Li-doped TAC and PLD-grown MoS_2 films. The spectra were obtained using a photon energy of 120 eV.

Fig. 15a shows the measured R(T) data in terms of log R vs T. For all our samples, the R(T) dependence tends to diverge as T decreases, which is characteristic of the insulating transport regime [29]. The undoped TAC-grown sample is far more resistive than the undoped PLD-MoS_2 one. After introducing the Li atoms in a PLD-MoS_2, the resistance increased quite dramatically with the increase of Li concentration. For the TAC-grown samples, the effect of Li doping on the resistance magnitude is considerably weaker. The same data are plotted as log R vs 1/T in Fig. 6.15b. It is evident that the data do not follow the Arrhenius dependence log R ∝ 1/T. such dependence is typical for the thermally activated transport and nearest neighbor hopping in disordered solids, which was observed previously in transport studies of MoS_2 [30].

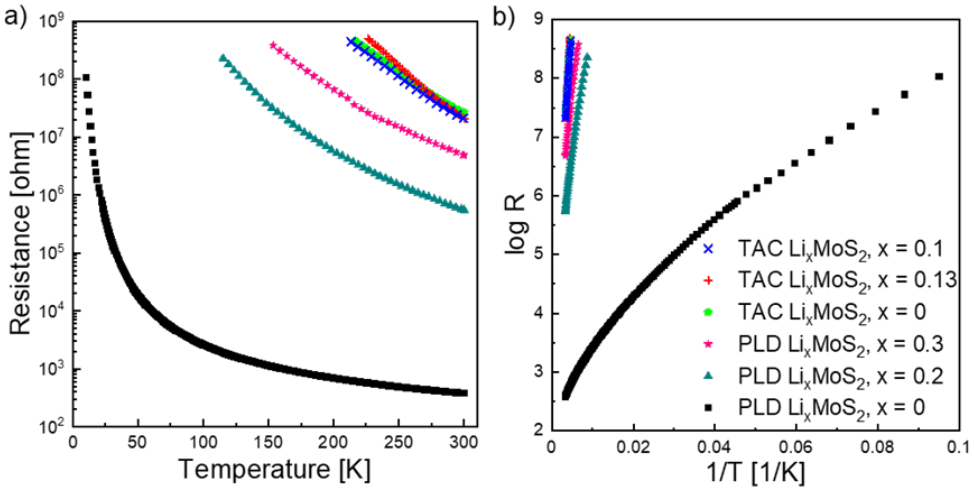

Figure 15: Measured R(T) dependence for a series of PLD-grown and TAC-grown MoS_2 thin films with corresponding Li stoichiometric coefficients. In panel (a) the data are shown as R vs T, and in panel (b) as log R vs 1/T.

At low enough temperatures, transport in disordered solids occurs via the Mott variable range hopping (VRH) rather than via the nearest neighbor hopping [29]. For the Mott VRH, the electron localized at the Fermi level (E_F) moves to another localized state in an optimum hopping distance which is determined by the trade-off between the lowest energy difference and the shortest hopping distance [29]. In a non-interacting disordered system, the density of states at the Fermi

level, $N(E_F)$, is finite and the resistance of the two-dimensional disordered system is described by Mott VRH with R(T) dependence $\ln(R/R_{Mott}) = (T_{Mott}/T)^{1/3}$, where

$$k_B T_{Mott} = \frac{27}{\pi N(E_F) L_{loc}{}^2}, \quad (1)$$

is the hopping activation energy, with L_{loc} being the electron localization length and $1/(N(E_F)L_{loc}{}^2)$ being the electron energy spacing the electron overcomes in one hop [29].

The Mott VRH dependence $\ln(R/R_{Mott}) = (T_{Mott}/T)^{1/3}$ has been observed at low temperatures in two-dimensional disordered MoS_2 flakes prepared by the exfoliation [30,31]. If the disordered film of interest is not sufficiently thin, the Mott VRH exhibits dependence $\ln(R/R_{Mott}) = (T_{Mott}/T)^{1/4}$, typical for three-dimensional systems [29].

Another work reported that the exfoliated MoS_2 flakes treated in n-butyllithium exhibit the dependence $\ln(R/R_{ES}) = (T_{ES}/T)^{1/2}$ [32], typical for the Efros-Shklovskii VRH [33]. Efros and Shklovskii have shown that the Coulomb interaction between the localized electrons opens the Coulomb gap at the Fermi level which emerges in the vanishing of $N(E_F)$. As a result, below a certain critical temperature the Mott VRH dependence $\ln(R/R_{Mott}) = (T_{Mott}/T)^{1/3}$ changes to the Efros-Shklovskii VRH dependence $\ln(R/R_{ES}) = (T_{ES}/T)^{1/2}$ with activation energy [33]

$$k_B T_{ES} = \frac{\Gamma e^2}{4\pi\varepsilon_r\varepsilon_0 L_{loc}}, \quad (2)$$

where e is the electron charge, ε_0 is the permittivity of vacuum, ε_r is the relative permittivity of the system, and $\Gamma = 6.5$ [34]. The Efros-Shklovskii dependence holds for any system dimensionality.

To determine which R(T) dependence applies to our samples, we plotted the data from Fig. 15 in Fig 6.16 as ln R vs $T^{1/2}$ and ln R vs $T^{1/3}$. For better visibility, the data are displayed separately due to different resistance magnitudes. The data in Fig. 6.16a for PLD-undoped samples support better the dependence $\ln(R/R_{ES}) = (T_{ES}/T)^{1/2}$; however, the data in Figs. 15b and 15c do not allow us to distinguish between $\ln(R/R_{ES}) = (T_{ES}/T)^{1/2}$ and $\ln(R/R_{Mott}) = (T_{Mott}/T)^{1/3}$, which is a frequently faced problem [34].

To demonstrate that all our samples follow the dependence $\ln(R/R_{ES}) = (T_{ES}/T)^{1/2}$, typical for Efros-Shklovskii VRH, we need to discuss the values of the fitting parameters T_{ES} and T_{Mott}. These parameters are summarized in Table 2 along with corresponding activation energies $k_B T_{ES}$ and $k_B T_{Mott}$. Firstly, we examine the TAC-grown samples and their values of T_{Mott}, which reach approximately 10^7 K, corresponding to activation energies $k_B T_{Mott} \sim 10^3$ eV. In contrast, the largest reported T_{Mott} value for MoS_2 films was about 10^5 K, corresponding to the activation energy $k_B T_{Mott} \sim 10$ eV [31]. Generally, activation energies for various thermally activated transport processes in disordered solids rarely exceed 10 eV. These activation energies are usually much lower [29]. Therefore, activation energies $k_B T_{Mott} \sim 10^3$ eV are too large to be meaningful, which leads us to the conclusion that our TAC-grown MoS_2 samples do not exhibit the Mott VRH, despite the R(T) data in Fig. 24c following the dependence $\ln(R/R_{Mott}) = (T_{Mott}/T)^{1/3}$ quite well. On the other hand, the values of T_{ES} are a hundred times lower and correspond to the activation energies $k_B T_{ES} \sim 7 - 12$ eV, which are quantitatively reasonable. So, we conclude that the undoped and Li-doped TAC-grown MoS_2 samples follow the Efros-Shklovskii VRH dependence $\ln(R/R_{ES}) = (T_{ES}/T)^{1/2}$.

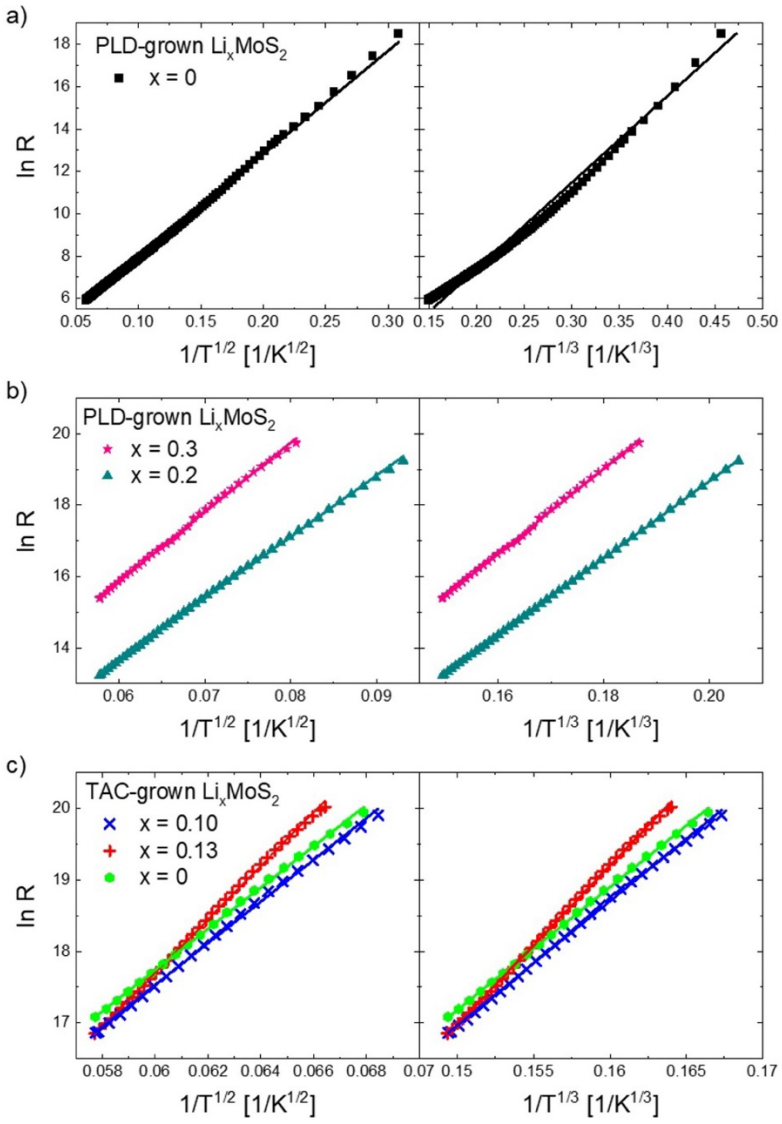

Figure 16: Experimental data from Fig. 15 are plotted as ln R versus $1/T^{1/2}$ and as ln R versus $1/T^{1/3}$. (a) Data for the undoped PLD-grown MoS_2 film, (b) data for the PLD-grown MoS_2 films with lithium stochiometric coefficients of x = 0.2 and x = 0.3, (c) data for the TAC-grown MoS_2 films without (x = 0) and with lithium doping (x = 0.1, x = 0.13). The solid lines show the fit of the experimental data by the dependencies $\ln(R/R_{ES}) = (T_{ES}/T)^{1/2}$ and $\ln(R/R_{Mott}) = (T_{Mott}/T)^{1/3}$. The values of the fitting parameters T_{ES} and T_{Mott} are summarized in Table 2.

The conclusion remains consistent also for the PLD-grown MoS_2 samples. In the case of the Li-doped PLD-grown samples shown in Fig. 24b, the activation energies k_BT_{Mott} (see Table 6.4) are still unusually high (above 10^2 eV), whereas the energies k_BT_{ES} reasonable (less than 3.5 eV).

Table 2: Studied MoS_2 samples, amount of Li_2S/S used for fabrication, stochiometric coefficient of Li, and composition determined by photoemission spectroscopy, fitting temperatures T_{ES}, T_{Mott}, and corresponding activation energies k_BT_{ES}, k_BT_{Mott}, characterizing the transport mechanism in the samples.

Sample	**Li_2S/S**	**Stoichiometric coefficient of Li - *x***	**Composition Li_xMoS_y**	**T_{ES} [K]**	**k_BT_{ES} [eV]**	**T_{Mott} [K]**	**k_BT_{Mott} [eV]**
TAC MoS_2	0%	0	$MoS_{2.2}$	82 942	7.1	5 049 152	435
TAC MoS_2	20%	x = 0.13 ± 0.03	$Li_{0.1}MoS_{2.2}$	84 772	7.3	5 240 436	451
TAC MoS_2	50%	x = 0.10 ± 0.02	$Li_{0.1}MoS_{2.2}$	140218	12.1	10 972 142	945
PLD MoS_2	0%	0	$MoS_{2.0}$	2 551	0.22	67 103	5.8
PLD MoS2	20%	x = 0.2 ± 0.1	$Li_{0.2}MoS_{2.1}$	29 503	2.54	1 252 645	108
PLD MoS2	50%	x = 0.3 ± 0.1	$Li_{0.3}MoS_{2.0}$	37 653	3.24	1 681 548	145

To support the above conclusions, we might plug $k_B T_{Mott} \sim 10^3$ eV into the equation (1) and obtain the energy level spacing $1/(N(E_F)L_{loc}^2 \sim 10^2$ eV, which is again too large to be meaningful. On the other hand, by plugging the activation energies $k_B T_{ES} \sim 0.22 - 12$ eV and permittivity $\varepsilon_r \sim 5$ (valid for few-layer MoS_2 films) to equation (2) we obtain the localization length $L_{loc} \sim 0.16 - 13$ nm. Here is even the lowest L_{loc} of 0.16 nm reasonably large and might correspond to a localized state at an impurity. According to this equation, the larger the activation energy $k_B T_{ES}$ the smaller the localization length L_{loc} due to disorder. If we examine $k_B T_{ES}$ values for undoped PLD-grown and TAC-grown MoS_2 samples (Tab. 2), we can see that TAC-grown MoS_2 has this value thirty times larger. Disorder in the undoped TAC-grown sample is therefore much stronger than in the undoped PLD-grown sample. The question remains what caused this strong disorder.

Looking closer at Tab. 2, we can see that TAC-grown MoS_2 samples are non-stoichiometric (the S:Mo ratio is about 2.2), while the PLD-grown MoS_2 samples have an S:Mo ratio close to 2. It is important to mention that excess sulfur does not affect the resulting XRD patterns demonstrating the crystalline arrangement. This indicates that the excess sulfur acts as an impurity disorder by filling the gaps between neighboring monolayers, leading to the significant electrical resistance observed in the TAC-grown samples.

What remains to be determined is the origin of the disorder in the undoped PLD-grown MoS_2 sample. We therefore estimated the lateral grain size distribution using atomic force microscopy. The size of grains L_{grains} for MoS_2 layers grown by TAC and PLD are in the range of 2 – 30 nm suggesting only negligible differences in grain sizes for these two fabrication methods. The undoped PLD–grown sample has a localization length L_{loc} of approximately 13 nm, which exceeds L_{grain}, suggesting that electron localization in the undoped PLD–grown sample is caused by disorder due to the grain boundaries. On the other hand, for the undoped TAC–grown sample is $L_{loc} \sim 0.3$ nm. Such a small L_{loc} cannot be ascribed to grain boundary disorder with L_{grain} in the range of 3 - 30 nm, therefore it must be attributed to the non-stoichiometry, as was discussed above. The disorder induced by the minor traces of impurities (Te, Na, K) detected via XPS is most probably negligible.

The fact that Li intercalation introduces additional disorder is visible in data from Table 2, as the increase of x is accompanied by the rise of $k_B T_{ES}$. Only one exception was observed – the TAC-grown sample with $x = 0.1$ exhibits a larger $k_B T_{ES}$ than the sample with $x = 0.13$. However, this inconsistency could be ascribed to experimental uncertainties in determining the Li concentration. If lithium caused any electron doping, such effect was completely obscured by the effect of disorder.

5.6 Doping effects in $PtSe_2$

Platinum diselenide is another member of the TMD material group that we have studied in the thesis. As we have already mentioned, $PtSe_2$ in the bulk form is semimetal becoming a semiconductor after thinning to a few layers. Thanks to the high values of charge carrier mobilities, this material is prospective for use in electronics. Our aim was to increase the charge carrier mobilities and to decrease the number of charge carriers to prepare the films suitable for field-effect transistors.

Li-doped $PtSe_2$ films were prepared in the same manner as Li-MoS_2. The part of selenium powder was replaced by lithium sulfide. Magnetron sputtered Pt layer layers (1 and 3 nm thick)

were annealed in a mixture of selenium with Li_2S powder. Since the growth temperatures of $PtSe_2$ are lower than those of MoS_2, annealing temperatures were in the range of 400 - 550 °C. Subsequently, films were characterized by Raman and electrical measurements. Raman measurements confirmed the formation of $PtSe_2$ after annealing with lithium presence. No significant difference was observed suggesting that the presence of Li in the reaction system did not influence the growth mechanism.

To estimate the charge carrier mobility, their number, and type of charge carriers, Hall effect measurements in van der Pauw configuration were performed. These measurements showed different behavior of the doped samples. Although the resistivity of the films increased, the results of the Hall measurements were inconclusive. This suggests the very low values of the charge carrier mobility. We suppose that this was caused by the disorder increase as in the case of Li-doped MoS_2. Thus, Li doping of $PtSe_2$ films is not suitable for the fabrication of the films for field-effect transistors. For that reason, we focused on the tuning of the selenium content in the samples.

Influence of Se content on charge carrier mobility

A set of $PtSe_2$ few-layer films was prepared by one-zone selenization of 1 nm thick pre-deposited Pt layers on the c-plane sapphire substrate. Annealing temperature (550 °C), heating rate (25 °C/min), and annealing time (30 minutes) were the same for the fabrication of each sample, while the nitrogen flow rate varied from 20 up to 350 sccm.

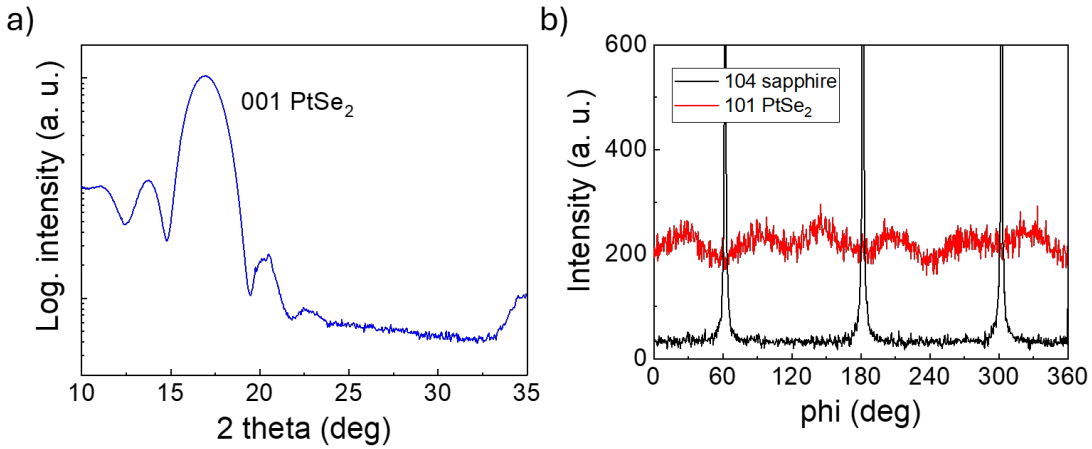

Figure 17: (a) Typical XRD pattern of the $PtSe_2$ film prepared by selenization of 1 nm Pt layer at 550 °C for 30 minutes and (b) φ-scan of 101 diffraction of $PtSe_2$ and 104 diffraction.

The crystal structure of as-prepared $PtSe_2$ films was determined by the XRD. The XRD patterns of various samples did not vary much with different nitrogen flow rates. In Fig. 17a is a typical XRD pattern obtained in symmetrical $\theta/2\theta$. Only a 001 diffraction of the hexagonal 1T $PtSe_2$ phase was present in the pattern, which suggests that layers are oriented horizontally. The Laue oscillations on both sides of dominant 001 diffraction demonstrate the films' high crystallinity and homogeneous thickness. The thicknesses of investigated $PtSe_2$ films were calculated from Laue oscillations and XRR measurements. All films have a similar thickness of 4 ± 0.5 nm, corresponding to 8 ± 1 monolayers of $PtSe_2$. In the azimuthal φ-scan of 101 diffraction of $PtSe_2$ are recognizable maxima, indicating a tendency of $PtSe_2$ layers to grow epitaxially (Fig. 17b).

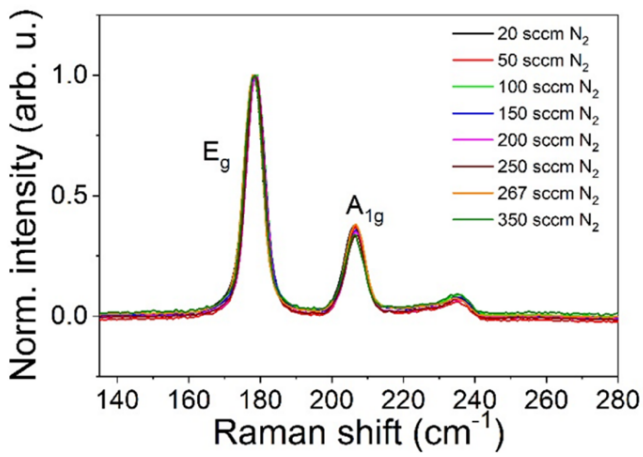

Figure 18: Normalized Raman spectra of $PtSe_2$ films prepared by selenization of 1 nm thick Pt layer at 550°C for 30 min with different nitrogen flow rates.

Normalized Raman spectra of all investigated $PtSe_2$ films are in Fig. 18. The vibrational modes belonging to $PtSe_2$ are visible in spectra, specifically, the E_g mode occurring around 175 cm^{-1} and the A_{1g} mode at approximately 207 cm^{-1}. The broad and less intense peak around 230 cm^{-1} is assigned to overlapping longitudinal optical modes [35].

The electrical characterization of our samples was done using the van der Pauw method without any patterning. The cold-pressed indium contacts were placed at the corners of the $PtSe_2$ samples. Results from the measurements are gathered in Table 3. The polarity of the Hall coefficient is positive for all as-prepared samples, suggesting the p-type of conductivity of our $PtSe_2$ films. The charge carrier mobility ranged from 10.8 to 27.1 $cm^2V^{-1}s^{-1}$ for the films prepared with different N_2 flow rates.

Table 3: Electrical properties of $PtSe_2$ films prepared by selenization of 1 nm Pt layer at 550 °C for 30 min with different N_2 flow rates and corresponding Se:Pt obtained by XPS analysis.

Nitrogen flow rate (sccm)	Hall mobility μ ($cm^2V^{-1}s^{-1}$)	Concentration of charge carriers (cm^{-2})	Hall constant (cm^2/As)	Se:Pt ratio (1200 eV)
20	20.3	1.1884×10^{14}	5.2522×10^4	2
50	14	1.7468×10^{14}	3.5731×10^4	1.971
100	15.4	1.4144×10^{14}	4.4130×10^4	1.979
150	23.19	8.30×10^{13}	7.50×10^4	2.002
200	18.1	1.4761×10^{14}	4.2283×10^4	1.988
250	27.1	1.0739×10^{14}	5.8122×10^4	2.035
267	24.4	6.72×10^{13}	9.29×10^4	2.015
350	10.8	3.5220×10^{14}	1.7722×10^4	1.971

However, there is no direct correlation between the charge carrier mobilities and nitrogen flow rates from Table 3. As the next characterization of $PtSe_2$ films, we have performed synchrotron-radiation XPS measurement using a photon energy of 1200 eV, to estimate the chemical composition of our layers. Fig. 19 shows typical binding spectra of Pt 4f and Se 3d. The binding energies of the main peaks at 73.07 ± 0.05 eV for Pt $4f_{7/2}$ and 54.40 ± 0.03 eV for Se $3d_{5/2}$ are in good agreement with previously reported values for $PtSe_2$ [35]. The Se:Pt ratio for our samples varies from 2.1 ± 0.2. These values differ for different Se:Pt ratios, moreover, we found

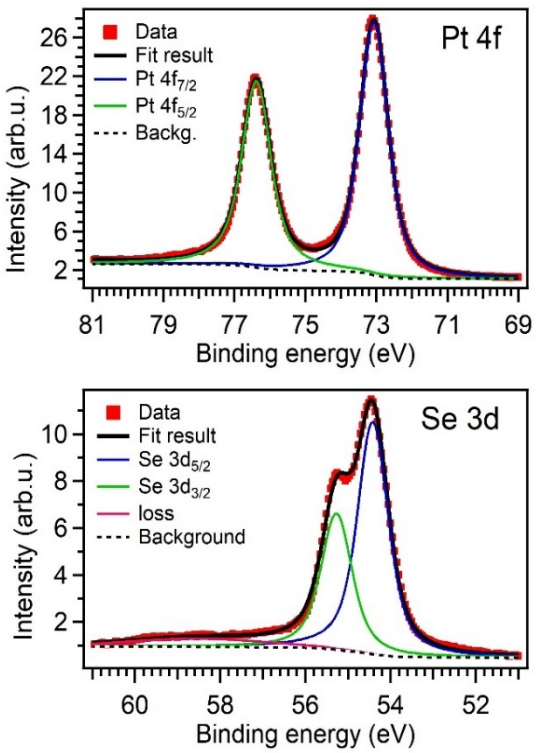

Figure 19: Typical XPS spectra (acquired at a photon energy of 1200 eV) of $PtSe_2$ films prepared by selenization of 1 nm thick Pt layer at 550 °C for 30 min

dependence of charge carrier mobility and concentration on the Se:Pt ratio. The mobility had increased more than twice as Se:Pt ratio increased in a relatively narrow range from 1.97 to 2.03. In contrast, the charge carrier concentration decreased at the same interval. This dependence is visualized in Fig. 20.

Such mobility vs. concentration is assigned to the scattering of charge carriers on ionized impurities. Thus, the smaller the concentration, the longer the scattering time and, consequently, the larger carrier mobility [36].

We can conclude that, although the nitrogen flow rate does not directly influence the structural and transport properties of the as-grown $PtSe_2$ films, we identified the Se:Pt ratio as the controlling parameter of the charge carrier mobility.

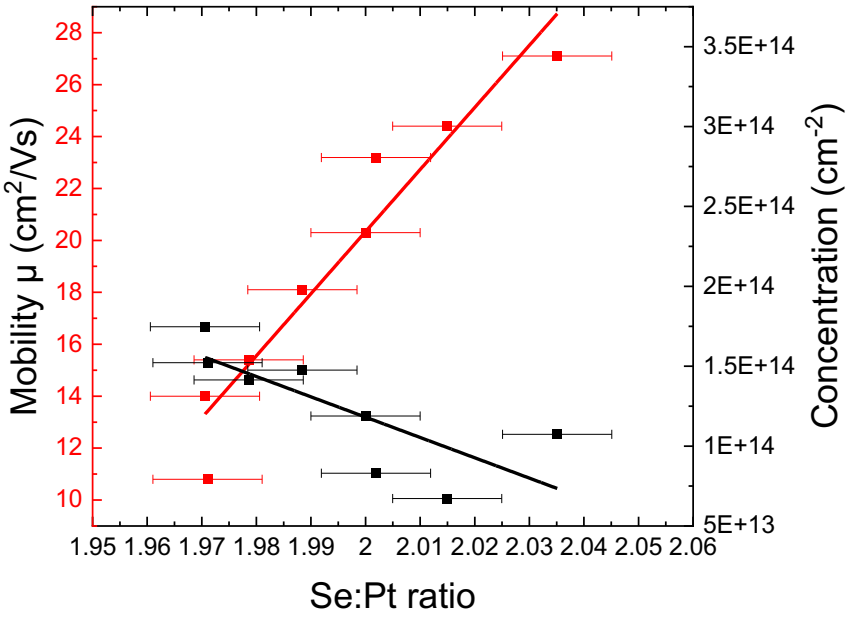

Figure 20: Se:Pt ratio dependence of charge carrier mobility and carrier concentration of $PtSe_2$. The solid lines represent linear fits to experimental values, and error bars correspond to uncertainty in XPS peak background removal.

6. Conclusions

Dissertation thesis was focused on the study, fabrication, and characterization of doped TMD films. Special attention was devoted to two promising TMD materials: MoS_2 and $PtSe_2$. Concretely, we focused on the fabrication and characterization of Li-doped MoS_2 and $PtSe_2$ layers and Se undoped/over-doped $PtSe_2$ layers. Few-layer films were prepared by thermally assisted conversion of pre-deposited metal layers. As prepared films were characterized by Raman spectroscopy, XRD, GIWAXS, AFM, ERDA, XPS, optical and electrical measurements.

Concerning Li-doped MoS_2, we used lithium sulfide (Li_2S) as the source of Li and two different initial layers – sputtered molybdenum and already-grown molybdenum disulfide layers of different thicknesses. The presence of Li was confirmed using synchrotron-radiation XPS with low photon energies and ERDA. Thanks to XPS and Li K-edge XANES we identified that Li intercalated into MoS_2 layers. We found out that the chosen method – one-zone sulfurization using Li_2S powder was suitable for preparing MoS_2 films containing Li. It was shown that Li-doping has a significant influence on the structural properties of MoS_2 layers, mainly on the orientation of the prepared layers. For thinner films (prepared from 1 nm Mo, or 4 nm MoS_2), ordering in a-b plane was observed in all cases. The thicker MoS_2 layers prepared by sulfurization have a predominantly vertical orientation. However, the 12 nm and 40 nm MoS_2 samples tend to grow horizontally or at least with mixed orientations when Li_2S was present in the annealing process. Moreover, an almost complete transition from vertical to horizontal alignment was observed for films prepared from 12 nm MoS_2 layers. Until now, the initial layer thickness and sulfur vapor pressure have been considered crucial parameters for the final orientation of MoS_2 layers grown by sulfurization. We demonstrated that the orientation of the MoS_2 basal plane in few-layer films can also be adjusted through lithium doping.

Li-doping or intercalation of MoS_2 might introduce the transition from the semiconducting 2H phase to the disordered 1T/1T′ phase. Raman spectroscopy, XRD, and optical absorption proved that our samples remained in the 2H phase after Li intercalation. We examined the electrical transport properties of horizontally aligned Li-doped MoS_2 layers. The initial MoS_2 layers were fabricated using two different methods- TAC and PLD. From electrical R(T) measurements we can conclude that all samples exhibited the insulating dependence $\ln(R/R_{ES}) = (T_{ES}/T)^{1/2}$, which is typical for the Efros–Shklovskii variable range hopping in a disordered semiconductor. The Li intercalation induced additional disorder enhancing the Efros–Shklovskii insulating regime of electronic transport already present in MoS_2 samples. The activation energies $k_B T_{ES}$ increased with the Li amount intercalated in the samples. The undoped TAC-grown MoS_2 sample was far more resistant than the undoped PLD-grown. The origin of the strong disorder in initial TAC-grown MoS_2 might be attributed to the sulfur non-stoichiometry (S:Mo ~ 2.2). On the other hand, the weak disorder in PLD-grown MoS_2 sample was due to the grain boundaries.

For $PtSe_2$ layers, the lithium intercorporation caused a disorder increase similar as in the case of MoS_2. However, our goal was to produce $PtSe_2$ layers suitable for the fabrication of FET transistor. Then we studied the influence of the nitrogen flow on structural, and electrical properties of prepared $PtSe_2$ layers, while other growing parameters (thickness of initial Pt layer, growing temperature, time, and heating rate) stayed unchanged. From the Raman, XRD, and XRR we saw no significant influence of nitrogen flow on the thickness and the crystal structure of as-

grown $PtSe_2$. Hall carrier mobility changed in range of 10.8 up to 27 $cm^2V^{-1}s^{-1}$, nonetheless, without any dependence on the nitrogen flow. XPS analysis revealed the difference in the stoichiometric Se:Pt ratio of investigated samples. Upon further examination, we saw clear correlation between the Se:Pt content in $PtSe_2$ layers and their carrier mobilities. The charge carrier mobilities increased with increasing Se:Pt ratio. At the same time the concentration of charge carriers decreased, meaning the scattering on the ionized impurities is likely the reason of observed dependence of mobility vs. Se:Pt ratio. We may conclude that even the nitrogen flow rate does not appear to control the structural and transport properties of as-grown films directly, we have identified the Se:Pt ratio as a parameter that controls the charge carrier mobility.

Published Papers (2021 – 2024)

2021

Shaji, A., Vegso, K., Sojková, M., Hulman, M., Nádaždy, P., Hutár, P., Pribusová Slušná, L., **Hrdá, J.**, Bodik, M., Hodas, M., Bernstorff, S., Jergel, M., Majková, E., Schreiber, F., and Šiffalovič, P.: **Orientation of few-layer MoS_2 films: in-situ x-ray scattering study during sulfurization**, J. Phys. Chem. C 125 (2021) 9461–9468.

Sojková, M., **Hrdá, J**., Volkov, S., Vegso, K., Shaji, A., Vojteková, T., Pribusová Slušná, L., Gál, N., Dobročka, E., Šiffalovič, P., Roch, T., Gregor, M., and Hulman, M.: **Growth of $PtSe_2$ few-layer films on NbN superconducting substrate**, Applied Phys. Lett. 119 (2021) 013101

Pribusová Slušná, L., Vojteková, T., **Hrdá, J.**, Pálková, H., Šiffalovič, P., Sojková, M., Vegso, K., Hutár, P., Dobročka, E., Varga, M., and Hulman, M.: **Optical characterisation of few-layer $PtSe_2$ nanosheet films**, ACS Omega 6 (2021) 35398-35403

Hrdá, J., Tašková, V., Vojteková, T., Pribusová Slušná, L., Dobročka, E., Píš, I., Bondino, F., Hulman, M., and Sojková, M.: **Tuning the charge carrier mobility in few-layer $PtSe_2$ films by Se: Pt ratio**, RSC Adv. 11 (2021) 27292.

2022

Shaji, A., Vegso, K., Sojková, M., Hulman, M., Nádaždy, P., Halahovets, Y., Pribusová Slušná, L., Vojteková, T., **Hrdá, J.**, Jergel, M., Majková, E., Wiesmann, J., and Šiffalovič, P.: **Stepwise sulfurization of MoO_3 to MoS_2 thin films studied by real-time X-ray scattering**, Applied Surface Sci 606 (2022) 154772.

Vegso, K., Shaji, A., Sojková, M., Pribusová Slušná, L., Vojteková, T., **Hrdá, J.**, Halahovets, Y., Hulman, M., Jergel, M., Majková, E., Wiesmann, J., and Šiffalovič, P.: **A wide-angle X-ray scattering laboratory setup for tracking phase changes of thin films in a chemical vapor deposition chamber**, Rev. Sci Instrum. 93 (2022) 113909.

2023

Kočí, M., Izsák, T., Vanko, G., Sojková, M., **Hrdá, J**., Szabó, O., Husák, M., Végsö, K., Varga, M., and Kromka, A.: **Improved gas sensing capabilities of MoS_2/diamond heterostructures at room temperature**, ACS Applied Mater. Interfaces 15 (2023) 34206-34214

Sojková, M., Píš, I., **Hrdá, J**., Vojteková, T., Pribusová Slušná, L., Vegso, K., Šiffalovič, P., Nádaždy, P., Dobročka, E., Krbal, M., Fons, P.J., Munnik, F., Magnano, E., Hulman, M., and Bondino, F.: **Lithium-induced reorientation of few-layer MoS_2 films**, Chem. Mater. 35 (2023) 6246-6257.

Pribusová Slušná, L., Vegso, K., Dobročka, E., Vojteková, T., Nádaždy, P., Halahovets, Y., Sojková, M., **Hrdá, J**., Precner, M., Šiffalovič, P., Chen, Z., Huang, Y., Ražnjević, S., Zhang, Z., and Hulman, M.: **Ordered growth of hexagonal and monoclinic phases of $MoTe_2$ on a sapphire substrate**, CrystEngComm 25 (2023) 5706-5713

Vojteková, T., Pribusová Slušná, L., Dobročka, E., Precner, M., Sojková, M., **Hrdá, J**., Gregor, M., and Hulman, M.: **Fourier-transform infrared spectroscopy of $MoTe_2$ thin films**, Phys. Status Solidi B 260 (2023) 2300250

2024

Hrdá, J., Moško, M., Píš, I., Vojteková, T., Pribusová Slušná, L., Hutár, P., Precner, M., Dobročka, E., Španková, M., Hulman, M., Chromik, Š., Šiffalovič, P., Bondino, F., and Sojková, M.: **Investigating structural, optical, and electron-transport properties of lithium intercalated few-layer MoS_2 films: Unraveling the influence of disorder**, Applied Phys. Lett. 124 (2024) 123101

List of Conferences

2021

Hrdá, J., Tašková, V., Vojteková, T., Pribusová-Slušná, L., Dobročka, E., Hulman, M., Píš, I., Bondino, F., and Sojková, M.: Selenium content influences the charge carrier mobility in few-layer $PtSe_2$ films – oral presentation at ADEPT 2021: 9th International Conference on Advances in Electronic and Photonic Technologies, Podbanské, High Tatras, Slovakia

2022

Hrdá, J., Vojteková, T., Pribusová-Slušná, L., Dobročka, E., Hulman, M., Píš I., and Sojková, M.: Influence of Li-doping on the structural properties of thin-layer MOS_2 films – opral presentation at ADEPT 2022 10th Inter. Conf. on Advances in Electron. Photon. Technol. – Tatranská Lomnica, High Tatras, Slovakia

Hrdá, J., Vojteková T., Pribusová Slušná, L., Dobročka, E., Vegso, K., Píš, I., Hulman, M., Precner, M., Chromik, Š., and Sojková, M.: Fabrication and study of lithium doped few-layer MoS_2 films prepared by one-zone sulfurization – poster presentation at EMRS 2022 Fall Meeting, Warsaw, Poland

2023

Hrdá, J., Vojteková, T., Pribusová Slušná, L., Dobročka, E., Vegso, K., Píš, I., Precner, M., Hulman, M., Chromik, Š., and Sojková, M.: Fabrication and characterization of lithium-doped few-layer MoS_2 films – poster presentation at 35th International Winterschool on Electronic Properties of Novel Materials (IWEPNM), Kirchberg, Austria

Hrdá, J., Moško, M., Vojteková, T., Pribusová Slušná, L., Precner, M., Hulman, M., Španková, M., Chromik, Š., and Sojková, M.: Electron transport in lithium-doped few-layer MoS_2 films – oral presentation at 11th Inter. Conf. on Advances in Electron. Photon. Technol. – ADEPT. Eds. D. Jandura et al. Žilina: EDIS 2023. ISBN 978-80-554-1977-0. P. 83-86.

Hrdá, J., Vojteková, T., Príbusová Slušná, L., Vegso, K., Pohorelec, O., Hulman, M., Gregušová, D. and Sojková, M.: High carrier mobility $PtSe_2$ thin films grown by one-zone selenization on various substrates – poster presentation at 2023 IEEE NAP 13th International Conference Nanomaterials: Applications & Properties, Bratislava, Slovakia

References

[1] Quhe R, Xu L, Liu S, Yang C, Wang Y, Li H, Yang J, Li Q, Shi B, Li Y, Pan Y, Sun X, Li J, Weng M, Zhang H, Guo Y, Xu L, Tang H, Dong J, Yang J, Zhang Z, Lei M, Pan F and Lu J 2021 Sub-10 nm two-dimensional transistors: Theory and experiment *Physics Reports* **938** 1–72

[2] Singh A K, Kumar P, Late D J, Kumar A, Patel S and Singh J 2018 2D layered transition metal dichalcogenides (MoS_2): Synthesis, applications and theoretical aspects *Applied Materials Today* **13** 242–70

[3] Novoselov K S, Geim A K, Morozov S V, Jiang D, Zhang Y, Dubonos S V, Grigorieva I V and Firsov A A 2004 Electric Field Effect in Atomically Thin Carbon Films *Science* **306** 666–9

[4] Bhimanapati G R, Lin Z, Meunier V, Jung Y, Cha J, Das S, Xiao D, Son Y, Strano M S, Cooper V R, Liang L, Louie S G, Ringe E, Zhou W, Kim S S, Naik R R, Sumpter B G, Terrones H, Xia F, Wang Y, Zhu J, Akinwande D, Alem N, Schuller J A, Schaak R E, Terrones M and Robinson J A 2015 Recent Advances in Two-Dimensional Materials beyond Graphene *ACS Nano* **9** 11509–39

[5] Kolobov A V and Tominaga J 2016 *Two-Dimensional Transition-Metal Dichalcogenides* (Cham: Springer International Publishing : Imprint: Springer)

[6] Chhowalla M, Shin H S, Eda G, Li L-J, Loh K P and Zhang H 2013 The chemistry of two-dimensional layered transition metal dichalcogenide nanosheets *Nature Chemistry* **5** 263–75

[7] Kuc A, Zibouche N and Heine T 2011 Influence of quantum confinement on the electronic structure of the transition metal sulfide T S 2 *Phys. Rev. B* **83** 245213

[8] Gong Y, Lin Z, Chen Y-X, Khan Q, Wang C, Zhang B, Nie G, Xie N and Li D 2020 Two-Dimensional Platinum Diselenide: Synthesis, Emerging Applications, and Future Challenges *Nano-Micro Letters* **12** 174

[9] Radisavljevic B, Radenovic A, Brivio J, Giacometti V and Kis A 2011 Single-layer MoS_2 transistors *Nature Nanotech* **6** 147–50

[10] Ahmed T, Zha J, Lin K K, Kuo H, Tan C and Lien D 2023 Bright and Efficient Light-Emitting Devices Based on 2D Transition Metal Dichalcogenides *Advanced Materials* **35** 2208054

[11] Yang D and Frindt R F 1996 Li-intercalation and exfoliation of WS2 *Journal of Physics and Chemistry of Solids* **57** 1113–6

[12] Yao J D, Zheng Z Q and Yang G W 2019 Production of large-area 2D materials for high-performance photodetectors by pulsed-laser deposition *Progress in Materials Science* **106** 100573

[13] Bosi M 2015 Growth and synthesis of mono and few-layers transition metal dichalcogenides by vapour techniques: a review *RSC Adv.* **5** 75500–18

[14] Sojková M, Vegso K, Mrkyvkova N, Hagara J, Hutár P, Rosová A, Čaplovičová M, Ludacka U, Skákalová V, Majková E, Siffalovic P and Hulman M 2019 Tuning the orientation of few-layer MoS_2 films using one-zone sulfurization *RSC Adv.* **9** 29645–51

[15] Lee J, Kim M J, Jeong B G, Kwon C, Cha Y, Choi S H, Kim K K and Jeong M S 2023 Electrical role of sulfur vacancies in MoS2: Transient current approach *Applied Surface Science* **613** 155900

[16] Xu H, Zhang H, Liu Y, Zhang S, Sun Y, Guo Z, Sheng Y, Wang X, Luo C, Wu X, Wang J, Hu W, Xu Z, Sun Q, Zhou P, Shi J, Sun Z, Zhang D W and Bao W 2019 Controlled Doping of Wafer-Scale $PtSe_2$ Films for Device Application *Adv. Funct. Mater.* **29** 1805614

[17] Loh L, Zhang Z, Bosman M and Eda G 2021 Substitutional doping in 2D transition metal dichalcogenides *Nano Res.* **14** 1668–81

[18] Liu J, Li B and Li Q 2022 Two-Dimensional Doped Materials *Magnetochemistry* **8** 172

[19] Wang Z, Li R, Su C and Loh K P 2020 Intercalated phases of transition metal dichalcogenides *SmartMat* **1** e1013

[20] Kappera R, Voiry D, Yalcin S E, Branch B, Gupta G, Mohite A D and Chhowalla M 2014 Phase-engineered low-resistance contacts for ultrathin MoS_2 transistors *Nature Mater* **13** 1128–34

[21] Zhao Y, Qiao J, Yu Z, Yu P, Xu K, Lau S P, Zhou W, Liu Z, Wang X, Ji W and Chai Y 2017 High-Electron-Mobility and Air-Stable 2D Layered $PtSe_2$ FETs *Advanced Materials* **29** 1604230

[22] Pariari D, Varma R M, Nair M N, Zeller P, Amati M, Gregoratti L, Nanda K K and Sarma D D 2020 On the origin of metallicity and stability of the metastable phase in chemically exfoliated MoS_2 *Applied Materials Today* **19** 100544

[23] Wang D and Zuin L 2017 Li K-edge X-ray absorption near edge structure spectra for a library of lithium compounds applied in lithium batteries *Journal of Power Sources* **337** 100–9

[24] Zhu G, Liu J, Zheng Q, Zhang R, Li D, Banerjee D and Cahill D G 2016 Tuning thermal conductivity in molybdenum disulfide by electrochemical intercalation *Nat Commun* **7** 13211
[25] Pribusová Slušná L, Vojteková T, Hrdá J, Pálková H, Siffalovic P, Sojková M, Végsö K, Hutár P, Dobročka E, Varga M and Hulman M 2021 Optical Characterization of Few-Layer $PtSe_2$ Nanosheet Films *ACS Omega* **6** 35398–403
[26] Ye M, Winslow D, Zhang D, Pandey R and Yap Y 2015 Recent Advancement on the Optical Properties of Two-Dimensional Molybdenum Disulfide (MoS_2) Thin Films *Photonics* **2** 288–307
[27] Aurbach D, Weissman I, Schechter A and Cohen H 1996 X-ray Photoelectron Spectroscopy Studies of Lithium Surfaces Prepared in Several Important Electrolyte Solutions. A Comparison with Previous Studies by Fourier Transform Infrared Spectroscopy *Langmuir* **12** 3991–4007
[28] Aurbach D, Pollak E, Elazari R, Salitra G, Kelley C S and Affinito J 2009 On the Surface Chemical Aspects of Very High Energy Density, Rechargeable Li–Sulfur Batteries *J. Electrochem. Soc.* **156** A694
[29] Mott N F and Davis E A 2012 *Electronic processes in non-crystalline materials* (Oxford: Clarendon Press)
[30] Qiu H, Xu T, Wang Z, Ren W, Nan H, Ni Z, Chen Q, Yuan S, Miao F, Song F, Long G, Shi Y, Sun L, Wang J and Wang X 2013 Hopping transport through defect-induced localized states in molybdenum disulphide *Nat Commun* **4** 2642
[31] Xue J, Huang S, Wang J-Y and Xu H Q 2019 Mott variable-range hopping transport in a MoS_2 nanoflake *RSC Adv.* **9** 17885–90
[32] Papadopoulos N, Steele G A and Van Der Zant H S J 2017 Efros-Shklovskii variable range hopping and nonlinear transport in 1 T / 1 T ′ − MoS_2 *Phys. Rev. B* **96** 235436
[33] Shklovskii B I, Efros A L and Luryi S 1984 *Electronic properties of doped semiconductors* (Berlin Heidelberg New York [etc.]: Springer-Verlag)
[34] Tsigankov D N and Efros A L 2002 Variable Range Hopping in Two-Dimensional Systems of Interacting Electrons *Phys. Rev. Lett.* **88** 176602
[35] O'Brien M, McEvoy N, Motta C, Zheng J-Y, Berner N C, Kotakoski J, Elibol K, Pennycook T J, Meyer J C, Yim C, Abid M, Hallam T, Donegan J F, Sanvito S and Duesberg G S 2016 Raman characterization of platinum diselenide thin films *2D Materials* **3** 021004
[36] Chattopadhyay D and Queisser H J 1981 Electron scattering by ionized impurities in semiconductors *Rev. Mod. Phys.* **53** 745–68